J. Fluid Mech. (1993), *vol.* 252, *pp.* 617–646

Unsteady confined buoyant plumes

By GILLES DESRAYAUD[1] AND GUY LAURIAT[2]

[1] IBM-France, C3NI, 95 rue de la Galéra, 34090 Montpellier, France

[2] Laboratoire de Thermique, CNAM, 292 rue Saint-Martin, 75141 Paris Cédex 03, France

(Received 7 October 1991 and in revised form 12 December 1992)

Two-dimensional time-dependent buoyancy-induced flows above a horizontal line heat source inside rectangular vessels, with adiabatic sidewalls and top and bottom walls maintained at uniform temperature, are studied numerically. Transitions to unsteady flows are performed by direct simulations for various depths of immersion of the source in the central vertical plane of air-filled vessels. For a square vessel and a line source near the bottom wall, the numerical solutions exhibit a sequence of instabilities, called natural swaying motion of confined plumes, beginning with a periodic regime having a high fundamental frequency followed by a two-frequency locked regime. Then, broadband components appearing in the spectra indicate chaotic behaviour and a weakly turbulent motion arises via an intermittent route to chaos. For rectangular vessels of aspect ratio greater than 2 and depths of immersion greater than the width, the flow undergoes a pitchfork bifurcation. This symmetry breaking is driven by the destabilization of an upper unstable layer of stagnant fluid above the plume. Then a subcritical Hopf bifurcation occurs. On the other hand, if the depth of immersion is lower than the width of the vessel, a stable layer of fluid is at rest below the line source. Then penetrative convection sets the whole air-filled vessel in motion and an oscillatory motion of very low frequency arises through supercritical Hopf bifurcation followed by a two-frequency locked state.

1. Introduction

Free laminar convection from a horizontal line heat source has been extensively investigated in the past. The classical self-similar solutions have been widely used in early theoretical studies (Fujii 1963; Gebhart, Pera & Schorr 1970; Fujii, Morioka & Uehara 1973; see also Gebhart *et al.* 1988, chap. 3 for a complete review), while the analysis have been extended to second-order (Hieber & Nash 1975) and third-order boundary-layer theory (Mörwald, Mitsotakis & Schneider 1986). During the same period, many experiments were conducted in air, water and silicone or spindle oil (Brodowicz & Kierkus 1966; Lyakhov 1970; Schorr & Gebhart 1970; Gebhart *et al.* 1970; Fujii *et al.* 1973; Nawoj & Hickman 1977). To explain the discrepancies between analytical and experimental results for centreline temperature and velocity distribution, the concept of a virtual line source has been considered by Forstrom & Sparrow (1967), Lyakhov (1970), Hieber & Nash (1975) and Yosinobu *et al.* (1979) in order to accommodate the divergence of the plume flow from ideal due to the finite diameter of the wire used to simulate the line source. However, this approach raised some controversies (Schorr & Gebhart 1970; Fujii *et al.* 1973; Nawoj & Hickman 1977) and did not account for all of the 15–20% differences between experiments and theoretical results; also, neither end conduction effects nor decrease of the plume velocity near both ends of the line source can account for these discrepancies. Yosinobu *et al.* (1979) attempted to explain them by heat loss under the wire due to

the fluid entrainment. But, Lyakhov (1970) found only a weak difference on bounding the space below the line source with an impermeable insulating plate, which is more consistent with the boundary-layer theory.

Forstrom & Sparrow (1967) were the first to observe a naturally swaying motion of the plume. This was confirmed by Schorr & Gebhart (1970) through flow visualization. Following these observations of regular swaying plumes, linear stability analysis of freely rising plumes based on quasi-parallel theory has been performed by Pera & Gebhart (1971) and later by Wakitani & Yosinobu (1984), but they failed to find a critical Grashof number. Haaland & Sparrow (1973) and Hieber & Nash (1975) obtained lower branches of neutral curves (and then critical Grashof numbers) by taking some non-parallel and higher-order effects of the base flow into account in the linear stability analysis. This indicates that two-dimensional disturbances are amplified selectively (see also Gebhart *et al.* 1988, chap. 11). More recently, Wakitani (1985) using a non-parallel theory (the WKB method) confirmed their results except for the amplification rate of disturbances within unstable regions. The experimental results of Bill & Gebhart (1975) for a plane plume subjected to naturally occurring disturbances and those of Pera & Gebhart (1971), Yosinobu *et al.* (1979) and Wakitani & Yosinobu (1984) for controlled disturbances confirmed the predictions of the linear stability analysis over a wide range of Rayleigh numbers. It has been demonstrated that sufficiently high-frequency disturbances are stable as they are convected downstream.

The transition from a laminar to a turbulent state in a freely rising plume has been experimentally investigated by Forstrom & Sparrow (1967), Bill & Gebhart (1975), Yosinobu *et al.* (1979) and Noto (1989), and in stable thermally stratified fluid inside a large enclosure by Noto, Matsui & Matsumoto (1982). Forstrom & Sparrow (1967) and Bill & Gebhart (1975) determined the beginning of the transition to be at Rayleigh numbers $Ra_X \approx 3.6 \times 10^8$ and $Ra_X \approx 8 \times 10^8$ respectively, while for an air plume Noto (1989) obtained $7 \times 10^7 \leqslant Ra_X \leqslant 1.4 \times 10^8$ from spectral analysis of thermocouple signals and change of the slope of the midplane temperature (the Rayleigh number is based on the vertical distance along the plume and the heat rate input). Noto (1989) found a swaying frequency of the thermal air plume proportional to the 0.4 or $\frac{1}{3}$ power of the heat rate depending on whether the plume reaches the ceiling of the enclosure in a laminar or a turbulent state, respectively. Eichhorn & Vedhanayagam (1982) determined analytically a power value of 0.3, which correlated their experimental results for a water turbulent plume within $\pm 10\,\%$. A $\frac{1}{3}$ power value was also found both by Urakawa, Morioka & Kiyota (1983) for the swaying frequency of a spindle oil plume with a free surface and by Wakitani & Yosinobu (1984) for a laminar air plume. Noto (1989) related the large discrepancies found in the critical Rayleigh number to the different methods used in its determination.

Also noted in the experiments of Eichhorn & Vedhanayagam (1982) and Urakawa *et al.* (1983) was a meandering motion. Indeed, experiences (performed in large rectangular enclosures) not only showed that the plume sways in a plane perpendicular to the wire but can also meander in the direction of the wire, i.e. across the span of the plume (Forstrom & Sparrow 1967; Fujii *et al.* 1973); however the underlying physical mechanisms are not yet clarified. Eichhorn, Lienhard & Chen (1974) and Incropera & Yaghoubi (1980) in experimental studies of immersed isothermal cylinders also observed 'transition from 2 to 3-dimensional instability, with increased the axial twisting or billowing'. This transition was attributed to fluid entrainment effects by Incropera & Yaghoubi (1980). When a meandering motion exists, these two periodic motions (meandering and swaying) are not independent of each other: the swaying motion is stable and only when the meandering waveforms along the heater are stable. This happens when the heater length equals integral multiples of a half-wavelength, the

meandering wave being a fairly precise sine curve (Eichhorn & Vedhanayagam 1982; Urakawa *et al.* 1983). The liquid surface height, linearly related to the meandering wavelength, and the length of the heater are the main parameters controlling the meandering waveform. It should be noticed that Pera & Gebhart (1971), Nawoj & Hickman (1977), Yosinobu *et al.* (1979), Noto *et al.* (1982) and Noto (1989) did not find any meandering motion in their experiments. Noto related, without experimental proof as it seems, the meandering motion to the width of the enclosure: meandering waveforms would appear only for small widths of enclosures.

Although considerable research efforts have been devoted to the study of self-similar solutions for freely rising plumes, they were confined inside vessels in many experimental investigations, in which the ascending fluid is cooled at a horizontal solid or free surface inducing a recirculating flow along sidewalls and an entrainment of underlying fluid. Despite the contributions of the foregoing experimental studies, much remains to be learned concerning the interaction of the plume motion with its surrounding, in particular with the top surface. To the authors' knowledge, no attempts have yet been made to numerically simulate thermal plumes inside rectangular vessels, except the recent ones of Peyret (1990) for double-diffusive convection and Zia, Xin & Zhang (1990) for an externally heated enclosure containing a local heat source of finite size. The restriction to two-dimensional flows precludes three-dimensional effects along the line source. Such a limitation is imposed by the computers presently available but a two-dimensional model is of interest to provide insight into the occurrence of the swaying motion and also into the transition from periodicity to chaos in considerable detail.

The formulation and the numerical method used in the present study of the dynamical and thermal behaviour of a plume above a line heat source immersed in a rectangular vessel is described in the following Section. The vessel has adiabatic sidewalls while the top and bottom surfaces are maintained at uniform temperature. Some insight in the stationary base flow regime for Rayleigh numbers just below the critical points is given in §3. The onset of oscillatory convection and subsequent time-dependent regimes in a square vessel are investigated in §4. Some preliminary results in square vessel have been presented in a short conference paper (Lauriat & Desrayaud 1990). We focus in §5 on penetrative convection which occurs in rectangular vessels for small depths of immersion of the source while symmetry-breaking bifurcation points and first oscillatory instabilities are presented in §6 for large depths of immersion.

2. Analysis

2.1. *Model equations*

The line source has been modelled as a local source term in the energy equation. This requires that the diameter of a real heat source be much smaller than the dimensions of the vessel.

We consider two-dimensional convection induced by a line heat source immersed at the point (x_s, y_s) in a Boussinesq fluid occupying a rectangular vessel of width D and depth $H (0 \leqslant x \leqslant D, 0 \leqslant y \leqslant H)$, referred to Cartesian coordinates with the y-axis pointing upwards. The third dimension of the vessel is taken to be sufficiently large that a two-dimensional approximation of the flow could be assumed valid. Thus, it is convenient to introduce the stream function ψ and the vorticity Ω such that:

$$V = (u, v) = \left(-\frac{\partial \psi}{\partial y}, \frac{\partial \psi}{\partial x} \right) \quad \text{and} \quad \Omega = -\Delta \psi, \tag{2.1}$$

where (u, v) are the components of the velocity in the (x, y) directions. Hence, the governing equations for the vorticity and the temperature are

$$\frac{\partial \Omega}{\partial t} + \nabla \cdot (\Omega V) = \nu_0 \Delta \Omega - g\beta \frac{\partial T}{\partial x}, \tag{2.2}$$

$$\frac{\partial T}{\partial t} + \nabla \cdot (TV) = \kappa_0 \Delta T + \epsilon', \tag{2.3}$$

where

$$\epsilon' = \frac{Q}{\rho_0 C_P} \delta(x_s - x)\, \delta(y_s - y) \tag{2.4}$$

is the thermometrical internal heating rate, Q the heat generated by unit length of the line source, κ_0, ν_0 are the thermal and viscous diffusivities, C_P the specific heat at constant pressure, ρ_0 the fluid density, β the coefficient of volume expansion and g the gravitational acceleration; the subscript 0 denotes thermophysical properties at the ambient temperature T_a. Also, $\delta(z)$ is the Dirac delta function and the integral of $\delta(x_s - x)\, \delta(y_s - y)$ over x and y equals unity if it includes $\delta(0)\, \delta(0)$, or, otherwise, is zero (Beck *et al.* 1988). Peyret (1990) used a similar technique but with an exponential decay of the intensity of the source term so that it could be represented accurately with a spectral decomposition.

Measuring distances and times in terms of the vessel width D and the thermal diffusion time D^2/κ_0, respectively, the dimensionless form of (2.1), (2.2) and (2.3) are

$$\Omega = -\Delta \psi, \tag{2.5}$$

$$\frac{1}{Pr}\left(\frac{\partial \Omega}{\partial t} + \nabla \cdot (\Omega V)\right) = \Delta \Omega - Ra \frac{\partial T}{\partial x}, \tag{2.6}$$

$$\frac{\partial T}{\partial t} + \nabla \cdot (TV) = \Delta T + \epsilon, \tag{2.7}$$

where $\epsilon = \delta(x_s - x)\, \delta(y_s - y)$. In the vorticity equation, Pr and Ra are respectively the Prandtl number and the Rayleigh number given by the relations

$$Pr = \nu_0/\kappa_0 \quad Ra = g\beta Q D^3/\lambda_0 \nu_0 \kappa_0.$$

The temperature is measured in terms of a characteristic temperature difference Q/λ_0, λ_0 being the thermal conductivity, and the ambient temperature T_a is chosen as the reference temperature.

Rigid, no-slip boundary conditions are imposed at the walls of the vessel. We assume that the upper and lower boundaries are maintained at the fixed temperature T_a, while the vertical boundaries are adiabatic. Thus, the dimensionless temperature satisfies the following boundary conditions:

$$\left.\begin{aligned} T = 0 \quad &\text{at } y = 0 \text{ and } A, \\ \partial T/\partial x = 0 \quad &\text{at } x = 0 \text{ and } 1, \end{aligned}\right\} \tag{2.8}$$

where $A = H/D$ is the aspect ratio of the cross-section of the vessel.

Ra	Grid	ψ_{max}	U_2	V_2	V_3	T_3
10^5	33×33	6.13	9.88	−12.46	36.54	0.140
	65×65	6.14	10.13	−12.75	36.58	0.141
	129×129	6.14	10.19	−12.83	36.59	0.141
10^6	33×33	18.52	43.55	−21.93	145.1	0.085
	65×65	18.53	44.59	−22.33	147.0	0.086
	129×129	18.56	44.87	−22.43	147.4	0.086
3×10^7	33×33	71.37	110.4	−41.80	640.4	0.041
	65×65	71.94	107.9	−42.15	675.5	0.044
	129×129	72.42	108.3	−41.57	684.9	0.045

TABLE 1. Comparison of some characteristic values for different Rayleigh numbers ($A = 1$, $H_s = 0.75$)

At steady state, the energy dissipated by the line source is lost at the boundaries. This requirement of equality leads to the non-dimensional steady-state condition:

$$\int_{\mathbb{D}} \delta(x_s - x)\,\delta(y_s - y)\,\mathrm{d}S = 1 = -\int_{\Gamma} \frac{\partial T}{\partial n}\,\mathrm{d}\Gamma, \tag{2.9}$$

where $\mathbb{D}$ is the problem domain and Γ the boundary. In addition, the heat flux through any horizontal plane, defined as

$$\phi(y) = \int_0^1 \left(-\frac{\partial T}{\partial y} + vT\right)\mathrm{d}x, \tag{2.10}$$

must satisfy the following conditions:

$$\phi(y^-) + \phi(y^+) = 1 \quad \forall y^- < y_s \quad \text{and} \quad \forall y^+ > y_s. \tag{2.11}$$

It is useful to introduce the mean kinetic energy $E_K = 1/(2\mathbb{D})\,\|V\|_{d,2}^2$ as a global measure of dynamics where $\|\ \|_{d,2}$ is the discrete L_2 norm.

2.2. *Numerical procedure*

The numerical technique employed in the present investigation has been described in Desrayaud, Lepeutrec & Lauriat (1990) and has been shown to be accurate and reliable for unsteady flows at very low Prandtl numbers. Here we shall mention only a few of its main features. The time integration of the vorticity and energy equations was performed using an alternating directional implicit (ADI) splitting scheme. The vorticity equation was then discretized by employing central differences based on Taylor series expansions for all spatial derivatives, including the convective terms. The nodal points were located on a standard mesh. For the energy equation, a control-volume formulation with staggered grids and central differencing was retained in order to improve the overall energy balance. One layer of grid points outside each boundary was included to facilitate the application of the boundary conditions using quadratic extrapolations. For both vorticity and energy equations, the Thomas algorithm was employed to solve the tridiagonal systems of algebraic equations. On the other hand, finite-difference equations for the stream-function equation were solved by a direct method which uses a block-cyclic reduction process. Such a direct, non-iterative solution procedure for the stream function was found to be essential for the present problem, i.e. to follow accurately unsteady motions. From the solution of the stream-function equation, the wall vorticities were updated using a second-order-accurate formulation.

Depth of immersion H_s	Grid	Source position	Ra	Frequency (± 0.12)
1.50	33×49	17, 13	2.5×10^4	2.07
	65×97	33, 25	2.5×10^4	2.07
1.00	33×49	17, 25	3×10^4	5.61
	65×97	33, 49	3×10^4	5.62
0.75	33×49	17, 31	3×10^5	15.17
	65×97	33, 61	3×10^5	15.14

TABLE 2. Frequencies for two uniform grids and for different depth of immersion in a rectangular vessel ($A = 2$)

A number of tests have been performed with various grid sizes and time steps to ensure accuracy, stability and avoid spurious aperiodic flows. Several test cases conducted to check that boundary-layer-like flows and plumes instabilities can be simulated accurately are shown in tables 1 and 2 for stationary and oscillatory regimes respectively. The results of computations carried out on 33×33, 65×65 and 129×129 uniform grids for $10^5 \leqslant Ra \leqslant 3 \times 10^7$ are reported in table 1 (subscripts 2 and 3 refer to the points $M_2(0.25, \frac{1}{2}A)$ and $M_3(0.5, \frac{3}{4}A)$). It can be seen that the solutions for the 65×65 and 129×129 grids are within 1% while the results could be considered as satisfactory for the coarsest grid.

Double-precision computations were found necessary for flows undergoing a Hopf bifurcation into time-dependent convection in order to avoid non-physical solutions and spurious wiggles in the dependent-variable fields. The flow was found to be stationary at $Ra = 3.1 \times 10^7$ when using a 65×65 grid, even though the computations were performed over more than 280000 time steps, and it became periodic at $Ra = 3.2 \times 10^7$. With a 129×129 grid the flow was found to be periodic at $Ra = 3.1 \times 10^7$. It is not surprising that the instabilities set in at lower Ra, because grid refinements shift bifurcation points slightly but without affecting their overall pattern.

For rectangular vessels of aspect ratio $A = 2$, 33×49 and 65×97 uniform grids have been used. In view of the moderate values of the Rayleigh number at which instabilities set in, it appears that a 33×49 grid is fine enough for $Ra < 10^6$ (table 2). A 66×97 grid was used for higher Rayleigh numbers.

Different dynamical regimes of the flow can be distinguished by examining high-resolution power spectra of some global or local fluctuating values. Since small time steps Δt are required to perform time integrations accurately (for example, a value of $\Delta t = 1.5 \times 10^{-5}$ was used at $Ra = 3.5 \times 10^7$), the data are oversampled. Hence, the data have been sampled every M points to yield a sufficient effective sampling period Δt_e. The Fourier transform has been estimated with a fast Fourier transform (FFT) algorithm and the FFT length has been chosen to be at least $N = 4096$ points to obtain good spectral resolution ($\Delta f = 1/N\Delta t_e$), spectral estimates being obtained up to the Nyquist frequency $f_N = 1/2\Delta t_e$. Power spectra have been normalized and plotted on a logarithmic vertical scale from 10^{-8} to 1.

3. Base-flow simulations

Typical results for the streamlines and isotherms are shown in figure 1(*a–c*) for various depths of immersion ($H_s = A - y_s$) of line sources in the central vertical plane of the vessels (i.e. $x_s = 0.5$). Maxima of the stream function are also given. All the simulations have been performed for air-filled vessels ($Pr = 0.71$).

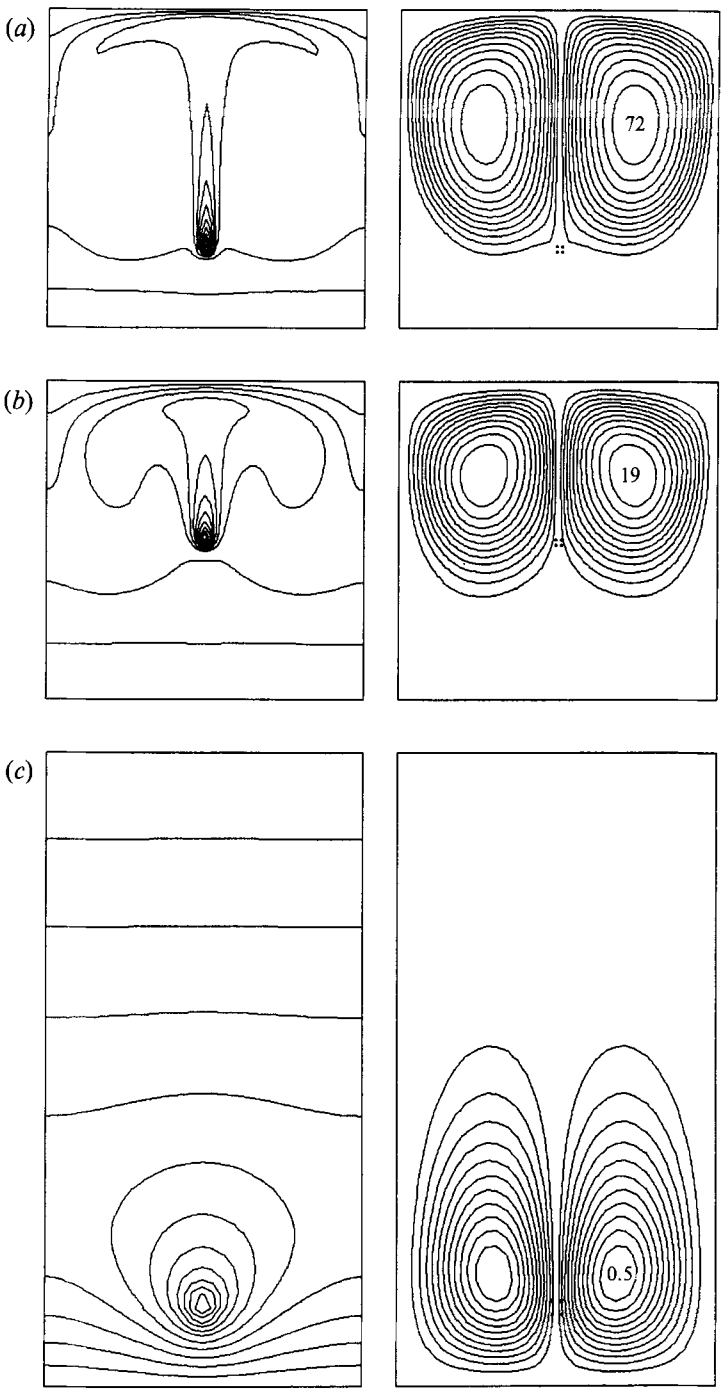

FIGURE 1. Steady-state isotherms and streamlines for various flows and Rayleigh numbers just below the critical values, $Pr = 0.71$. (*a*) $Ra = 3 \times 10^7$, $A = 1$, $H_s = 0.75$; (*b*) $Ra = 1.9 \times 10^6$, $A = 1$, $H_s = 0.50$; (*c*) $Ra = 5 \times 10^3$, $A = 2$, $H_s = 1.75$.

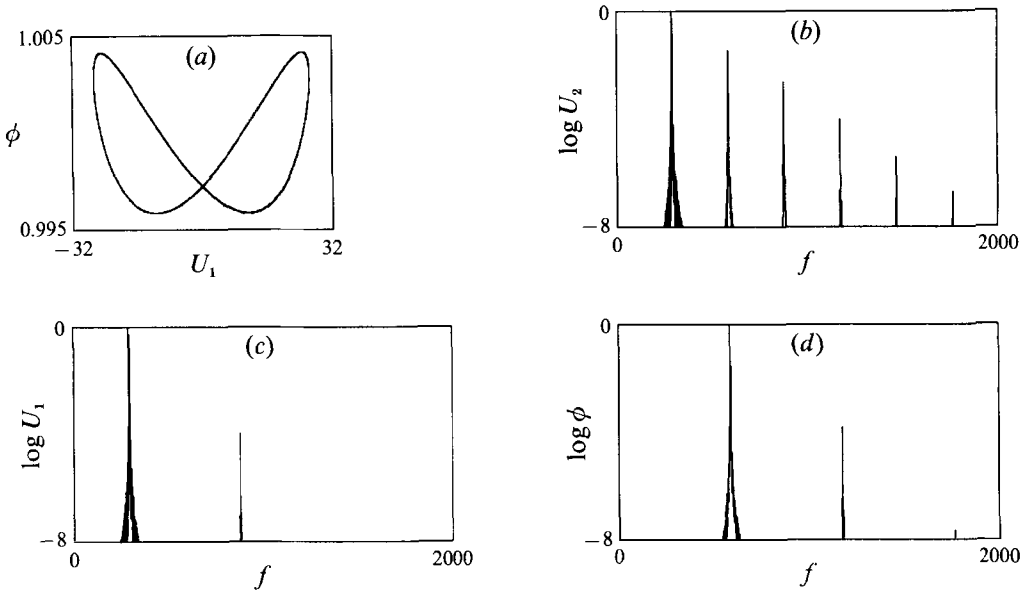

FIGURE 2. Periodic flow of frequency $f = 294.2 \pm 0.4$ in a square vessel for $Ra = 3.1 \times 10^7$, $H_s = 0.75$. (*a*) Phase portrait of the horizontal component of the velocity U_1 at point $M_1(\frac{1}{2}, \frac{2}{3}A)$ versus upper heat flux ϕ. (*b*) Power spectrum of the horizontal component of the velocity U_2 at point $M_2(\frac{1}{4}, \frac{1}{2}A)$. (*c*) Power spectrum of the horizontal component of the velocity U_1. (*d*) Power spectrum of upper heat flux ϕ.

(*a*)	H_s	Ra_1 Ra_2	f	Type of Hopf bifurcation
	0.75	$(3.0\text{–}3.1) \times 10^7$	294.2	Supercritical
	0.50	$(1.5\text{–}1.6) \times 10^6$	30.4	Supercritical
	0.25	$(3.1\text{–}3.2) \times 10^6$	38.5	Supercritical
(*b*)	H_s	Ra_1 Ra_2	f	Type of Hopf bifurcation
	1.75	$(3.00\text{–}3.02) \times 10^4$	0.2	Subcritical
	1.50	$(2.1\text{–}2.2) \times 10^4$	1.7	Subcritical
	1.25	$(1.0\text{–}1.5) \times 10^4$	1.9	Subcritical
	1.00	$(2.0\text{–}2.5) \times 10^4$	5.3	Supercritical
	0.75	$(2.5\text{–}3.0) \times 10^5$	15.0	Supercritical
(*c*)	A	Ra_1 Ra_2	f	Type of Hopf bifurcation
	2.00	$(2.5\text{–}3.0) \times 10^5$	15.0	Supercritical
	1.75	$(3.0\text{–}4.0) \times 10^5$	17.2	Supercritical
	1.50	$(8.0\text{–}9.0) \times 10^5$	25.6	Supercritical
	1.25	$(1.0\text{–}1.5) \times 10^6$	33.2	Supercritical
	1.00	$(3.0\text{–}3.1) \times 10^7$	294.2	Supercritical

TABLE 3. Critical Rayleigh numbers, frequency and type of Hopf bifurcation at various depths of immersion for (*a*) $A = 1$ and (*b*) $A = 2$ and (*c*) for various aspect ratios at $H_s = 0.75$

Table 3 gives the lower and upper bounds on the critical Rayleigh numbers. These bounds are for the highest value at which a steady-state motion was found to exist (Ra_1) and the smallest value at which the flow was found unsteady (Ra_2). The frequencies reported in table 3 are for the Ra_2-values. The different types of bifurcation

occurring in the configurations considered are given also. Steady-state isotherms and streamlines in square and rectangular vessels for Rayleigh numbers just below the first bifurcation point are displayed in figure 1. It can be seen that a recirculation flow is induced in which hot fluid rises with the plume above the line source, is cooled downstream and then descends along both sides of the vessel. The flow fields are characterized by mirror symmetry about the vertical centreline. It is seen from figure 1(*a*) ($A = 1, H_s = 0.75$) that for line sources near the bottom wall, a strong steady fluid circulation occurs above the line source while a relatively stagnant layer of fluid is seen below. Obviously, the temperature gradients inside the bottom region strongly depend on the thermal boundary conditions applied at the bottom wall, while the flow and temperature fields in the upper region of the vessel are weakly affected by this thermal boundary condition provided the Rayleigh number is large enough (Lauriat & Desrayaud 1990). Similar features are seen in figure 1(*b*) for smaller depth of immersion, $H_s = 0.5$, but the bottom stagnant layer of fluid which is stably stratified now extends over one-third of the vessel approximately. On the other hand, for large depth of immersion in rectangular vessels as shown on figure 1(*c*), the plume does not reach the top wall and there is an unstably stratified layer of stagnant fluid above the plume. It should be noticed that the fluid circulation is very weak owing to the low Rayleigh number. The flow is in a conductive state, as confirmed by the quasi-circular isotherms around the source.

These three flow patterns give way to three different routes to chaos. The first scenario, studied in the next section, can be found only if the layer of fluid below the line source is small enough and if the plume reaches the top of the vessel. This happens only in vessels of small aspect ratio ($A \leqslant 1$). The resulting periodic motion can be viewed as the natural swaying motion of confined plumes in the sense that the instabilities are neither driven by a stable layer of fluid at rest below the source as on figure 1(*b*) nor triggered by an unstable layer of fluid above the plume as on figure 1(*c*). In the present study, these two other scenarii are called penetrative convection, since the convecting plume is bounded below by a conducting layer of fluid, and Rayleigh–Bénard-like convection, since the underlying mechanism of the onset of instabilities is the destabilization of a motionless upper layer. These two mechanisms are respectively studied in §§5 and 6.

Thus, contrary to what has been found in many studies in freely rising thermal plume, interactions of the plume with the top and side walls play a dominant role in the flow structure.

4. Natural swaying motion in a square vessel

In this section the numerical results discussed are for vessels of square cross-section, the line source being near the cold bottom wall ($H_s = 0.75$) as in figure 1(*a*).

4.1. *Periodic motion*

For Rayleigh numbers lower than $Ra_c = 3 \times 10^7$, the system is attracted to a fixed point, representing a steady motion. The bifurcation leads to a system which is then attracted to a limit cycle, indicating a periodic motion. Figure 2 shows four plots of data for $Ra = 3.1 \times 10^7$, for which a periodic asymptotic state is reached at $t \approx 5$ ($\Delta t = 5 \times 10^{-5}$). The first plot presents the phase portrait of (U_1, ϕ) while the other three are for spectral densities of the horizontal component of the velocity at two points and the heat flux through the upper boundary (ϕ). The data shown on figure 2(*a*) are for every time step during the time interval $7 \leqslant t \leqslant 8.75$ with 68 iterations per cycle,

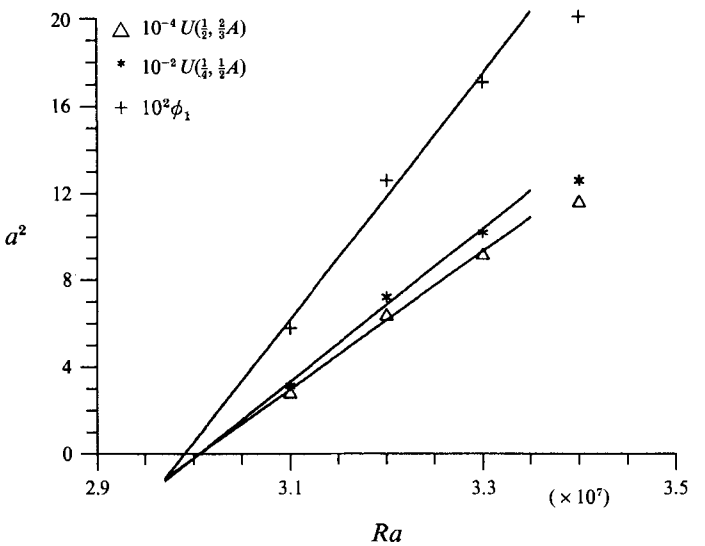

FIGURE 3. Variations of the squared amplitudes of fluctuations for horizontal components of the velocity U_1 and U_2 and upper heat flux ϕ in the left-half of the vessel.

$10^{-7}Ra$	Description	Frequency	$Ra^{\frac{1}{2}}/f$
3.00	Supercritical Hopf bifurcation		
3.10	P1	$f_1 = 294.2$	18.93
3.20	P1	$f_1 = 299.7$	18.87
3.30	P1	$f_1 = 305.2$	18.82
3.40	Transient QP2, then P1	$\begin{cases} f_1 = 310.1 \\ (f_2 = 94.4) \end{cases}$	18.80
3.50	Transient QP2, then P1	$\begin{cases} f_1 = 314.8 \\ (f_2 = 96.1) \end{cases}$	18.79
3.60	Transient QP2, then P1	$\begin{cases} f_1 = 319.4 \\ (f_2 = 97.7) \end{cases}$	
3.70	P2T (weak f_0)	$\begin{cases} f_1 = 323.5 \\ f_2 = 99.2 \end{cases}$	
3.80	P2T (weak f_0)	$\begin{cases} f_1 = 328.2 \\ f_2 = 101.1 \end{cases}$	
3.85	Transient P2T, then I		
3.90	Transient P2T, then I		
4.00	I		

TABLE 4. Route to chaotic motion in a square vessel with a line source at $H_s = 0.75$: P1, periodic state; QP2, Quasi-periodic state with two incommensurate frequencies; PT2, periodic state on a 2-torus; I, intermittent state

representing slightly less than 515 cycles. Figure 2(*a*) clearly illustrates the precisely periodic nature of an asymptotic flow, the fundamental frequency of which is $f_1 = 294.2$ as shown in figure 2(*b*). Only odd harmonics are present for U_1 in figure 2(*c*) while the fundamental frequency and odd harmonics are missing for ϕ in figure 2(*d*); these plots indicate a symmetry in the motion during the period, which is also depicted on figure 2(*a*).

Moreover, we noticed that the closer to the critical value the Rayleigh number is, the longer is the time for attaining the asymptotic flow. This suggests that the onset of

(*a*)

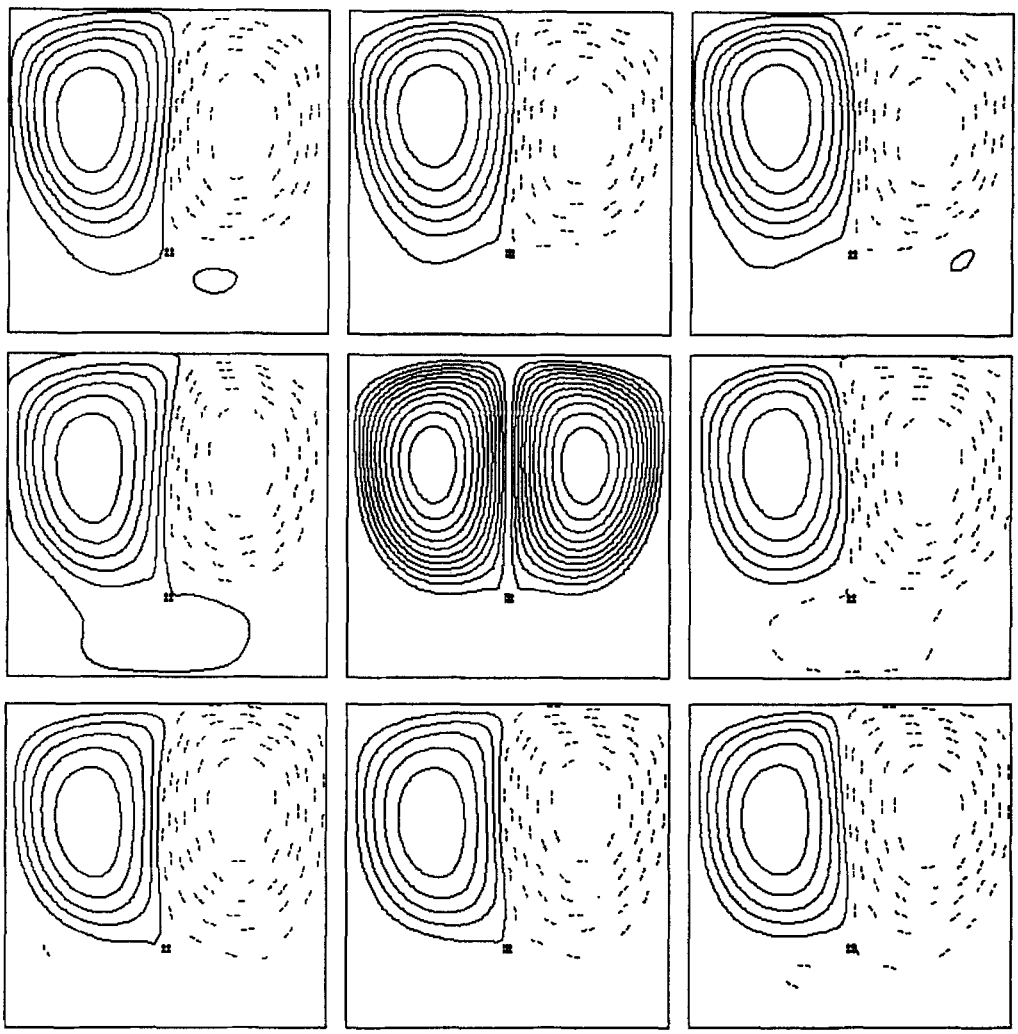

FIGURE 4(*a*). For caption see page 629.

unsteady solutions is due to the presence of a Hopf bifurcation point. Indeed, for such a bifurcation, the time needed to reach the asymptotic flow behaves like $(Ra-Ra_c)^{-1}$. Figure 3 shows that the amplitude of the perturbation for slightly supercritical Rayleigh numbers evolves like $(Ra-Ra_c)^{\frac{1}{2}}$, which is also the signature of a Hopf bifurcation (Bergé, Pomeau & Vidal 1988). This feature has been used to accurately determine the value of the critical point, which has been done from linear extrapolation of zero oscillation amplitude occurring close to the presumed threshold value. The squares of the amplitudes of the fluctuations, shown in figure 3 for U_1, U_2 and ϕ_1 for various supercritical Rayleigh numbers, give a critical Rayleigh number very close to 3×10^7. In addition, it has been found that the flow undergoes a supercritical Hopf bifurcation since no hysteresis effect has been encountered on decreasing the Rayleigh number from 3.1×10^7 to 2.9×10^7. A further feature of a Hopf bifurcation is the existence of a relationship between the dimensionless period of the oscillations and the Rayleigh number in the vicinity of the bifurcation point. By noting that the two cells

(*b*)

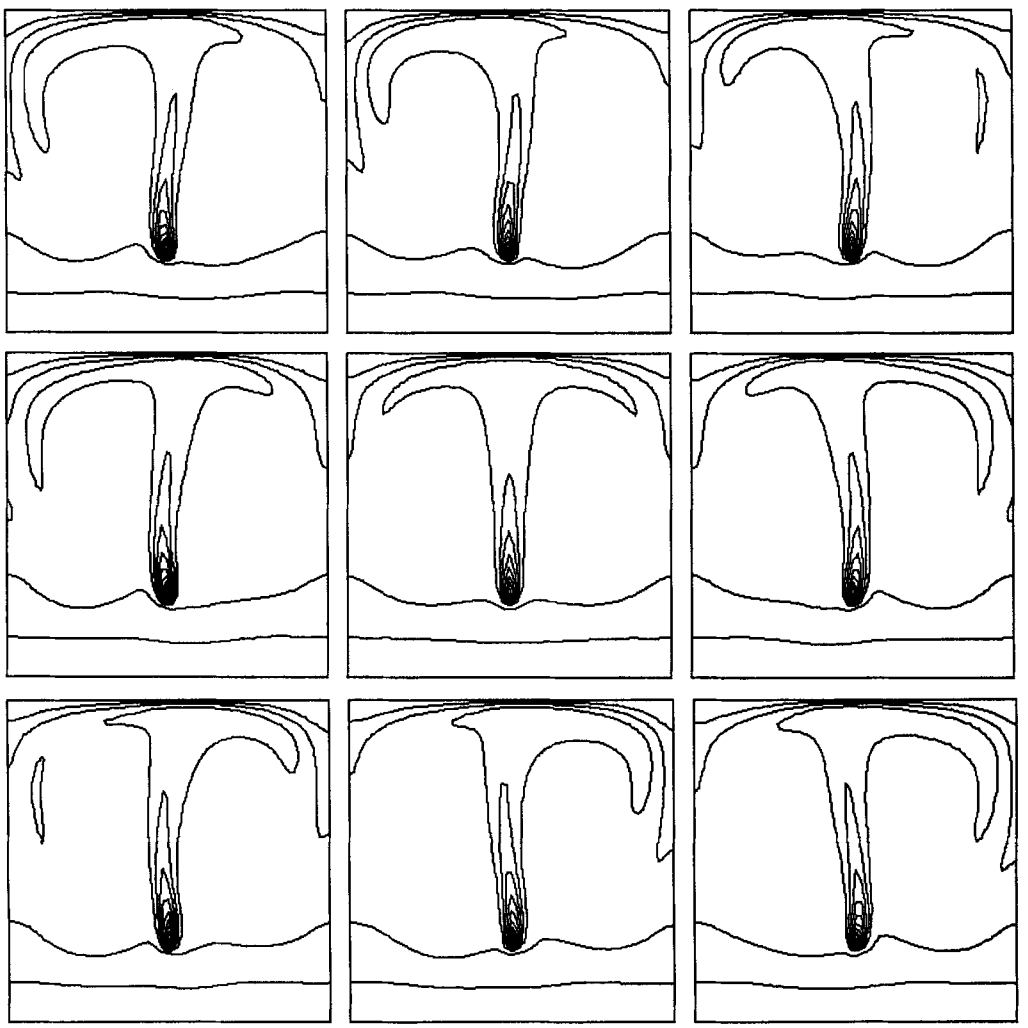

FIGURE 4(*b*). For caption see facing page.

on each side of the thermal plume have a relatively stagnant and unstably stratified core, we could calculate the angular Brunt–Vaïsälä frequency N associated to the plume because, for high Rayleigh numbers, the heat is mainly transferred to the top wall. Then, for any horizontal planes above the heat source

$$Q/D \approx \lambda_0 \partial T/\partial y$$

$$N^2 = \left[\frac{N'D^2}{\kappa_0}\right]^2 = -\frac{g}{\rho}\frac{\partial \rho}{\partial y}\frac{D^4}{\kappa_0^2} = g\beta\frac{\partial T}{\partial y}\frac{D^4}{\kappa_0^2} = Ra\,Pr.$$

Thus, the frequency is proportional to $N = (Ra\,Pr)^{\frac{1}{2}}$ and should be nearly constant near the threshold. This is well supported by the results shown in table 4. All the frequencies given in table 4 have also been calculated with a smaller time step (generally half the previous one) to check that the asymptotic flow dynamics are independent of the time step.

(*c*)

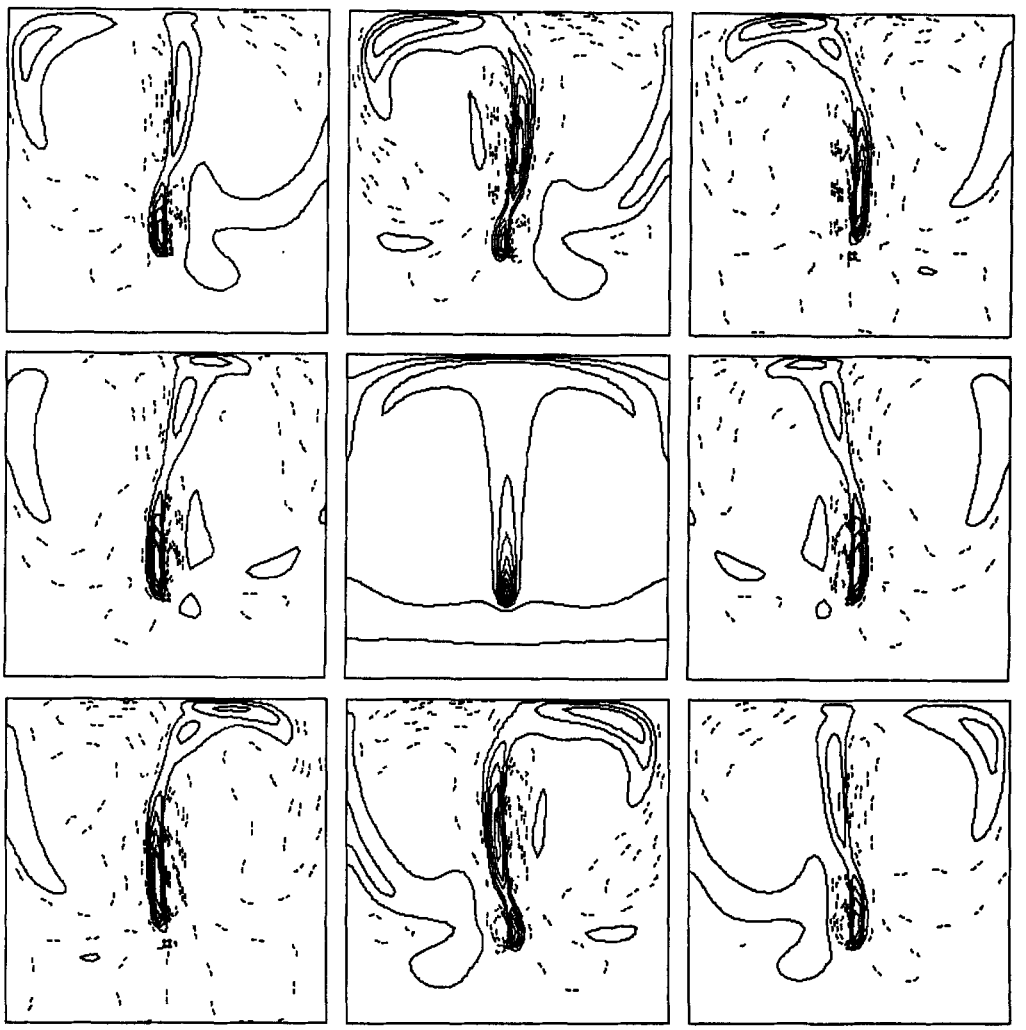

FIGURE 4. (*a*) Streamlines, (*b*) isotherms and (*c*) disturbance isotherms plotted over one oscillation period, with the base state at the centre, for $Ra = 3.5 \times 10^7$, $A = 1$, $H_e = 0.75$.

A second frequency f_2 (given in parentheses in table 4) appears at $Ra = 3.4 \times 10^7$ during the transient evolution but vanishes for a time unit greater than one, meaning that the frequency f_2 has at least eight orders of magnitude less power; moreover, these two frequencies are incommensurate.

The isotherms and streamlines are shown for $Ra = 3.5 \times 10^7$ in figures 4(*a*) and 4(*b*) over one period for eight snapshots equally spaced in counterclockwise progression around the figure at the centre. The base-state streamlines (*a*) and isotherms (*b*, *c*) are plotted at the centre of figure 4. Positive and negative values of the streamlines correspond to counterclockwise (solid lines) and clockwise (dashed lines) circulations respectively. The periodic motion and the symmetry with respect to the vertical centreplane during one period are clearly visible. These findings were experimentally recorded by Yosinobu *et al.* (1979) in the case of a buoyant plume in air. The general pattern of the mean temperature and stream function fields calculated are given in the

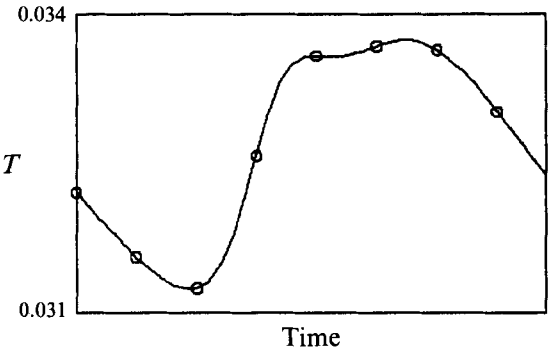

FIGURE 5. Evolution of the temperature at point $M(0.828, 0.875)$ over one oscillation period. Open circles are for frames of figure 4.

centre part of figure 4(*a*, *b*) and are the same as those presented in figure 1(*a*), but with higher isovalues. It can be seen that the upper part of the plume has the same symmetrical motion, once to the left, once to the right of the cavity. Consequently, the frequency of the heat flux at the top wall is twice the fundamental frequency (see also figure 2*d*). Figure 4(*c*) presents a time sequence of the fluctuating temperature field corresponding to the global field shown in figure 4(*b*). This fluctuating field has been calculated by taking the mean arithmetic field over one period and then subtracting it from instantaneous fields once the asymptotic periodic motion has been reached. It can be seen in figure 4(*c*) that hot and cold fluctuations grow simultaneously on each side of the source and a circulation of alternately hot and cold fluctuations arises in the two halves of the vessel. The instabilities are first confined within the plume where they are amplified and within the horizontal boundary layer near the top wall, then they move downward and back to the heat source. Therefore, instead of a swaying motion with sinusoidal wavelength as for a freely rising plume, we observed two counter-rotating circulations of fluid with alternating hot and cold spots. The motion of the plume itself is rather weak and detached blobs arise in the upper horizontal extents of the plume and sink along the vertical adiabatic surface. This behaviour is supported by the record of the temperature in the upper right corner of the vessel (point with coordinates (0.828, 0.875)) shown on figure 5 which displays the appearance of one blob during the period. Urakawa *et al.* (1983) experimentally found identical behaviour in spindle oil but with a much stronger motion of the plume, especially just above the line source.

4.2. *Two-frequency locked state*

For $3.7 \times 10^7 \leqslant Ra \leqslant 3.8 \times 10^7$, the motion smoothly becomes a periodic, two-frequency locked state involving the f_1 and f_2 frequencies. The asymptotic state is then a limit cycle on a 2-torus of small cross-section which can be seen on the phase portrait of the upper heat flux versus U_1 over one fundamental period (figure 6). The phase portrait reveals that the trajectories are confined to a finite number of threads. The Poincaré section (not shown here) confirms this behaviour since 13 distinct group points are visited in turn: for 13 rotations about its larger dimension, the trajectories pass four times around the smaller dimension. Thus, the rotation number (or the frequency-locking ratio) is $r = \frac{4}{13}$ and the fundamental frequency equals $f_0 = \frac{1}{13} f_1 = \frac{1}{4} f_2$. This is well supported by the frequency values reported in table 2. It should be noted that the spectral resolution does not allow us to determine f_1/f_2 with an accuracy better than 0.03; at $Ra = 3.7 \times 10^7$, it has been found that $f_1/f_2 = 3.26 \pm 0.03 \approx \frac{13}{4}$. By filtering out the flow evolution over one fundamental period $P_0 = 1/f_0$ with the shorter

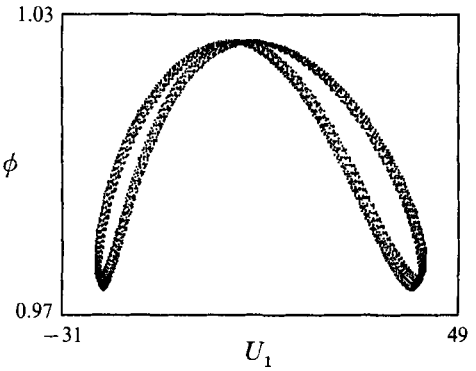

FIGURE 6. Phase portrait of the upper heat flux ϕ versus U_1 over one fundamental period P_0, $Ra = 3.8 \times 10^7$, $A = 1$, $H_a = 0.75$.

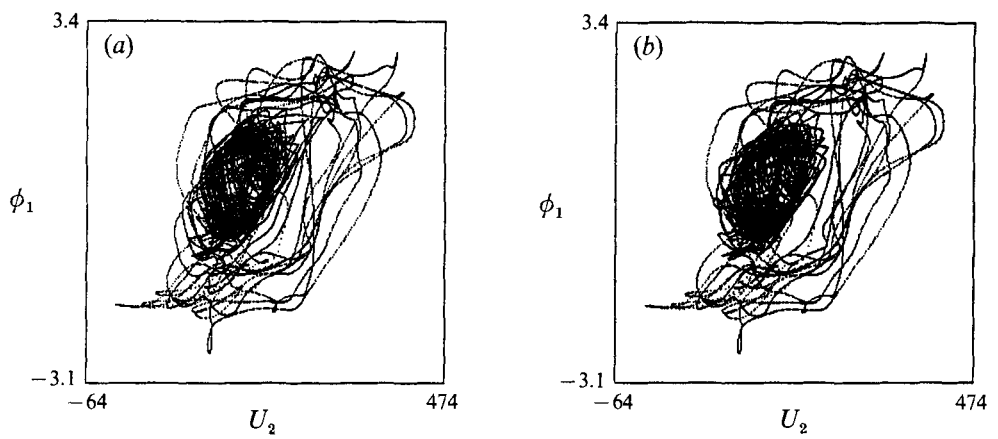

FIGURE 7. Phase portrait (ϕ_1, U_2) of the intermittently chaotic state ($Ra = 3.85 \times 10^7$) arising from the frequency-locked state ($Ra = 3.80 \times 10^7$): (*a*) laminar motion + first burst period; (*b*) first burst period + first relaminarization period.

frequency f_2, we obtain the same (apparent) motion as that presented in figure 4; only the f_1-frequency motion is then visible. If the evolution is now filtered out with the largest frequency f_1, only a very weak f_2-frequency motion is then visible, confined in the centre of the two cells. This weak influence of the f_2-frequency is illustrated by the slenderness of the 2-torus in figure 6. It should also be noticed that the nonlinearities are weak since the contribution of the low-order mixing components (f_1,f_2) is small. Simulations have been carried out up to 150000 time steps ($t > 3$), and no established quasi-periodic motion (f_1,f_2 incommensurate) has ever been found.

4.3. *Chaos*

An intermittently chaotic state arises from the previous frequency-locked state. At irregular times and for irregular durations, the periodic laminar motion is interrupted by non-periodic 'bursts'. However, the characteristic of the frequency-locked state with locking ratio $\frac{4}{13}$ is maintained in the laminar windows. As a result, the spectrum exhibits broadband noise although relatively sharp spectral peaks still exist for all frequency multiples of the $\frac{4}{13}$ locked state. Figure 7(*a*) shows the phase portrait during the end of the laminar transition and the first burst period for the time point interval [175000–203000]. The trajectories are confined to a small region in the phase space

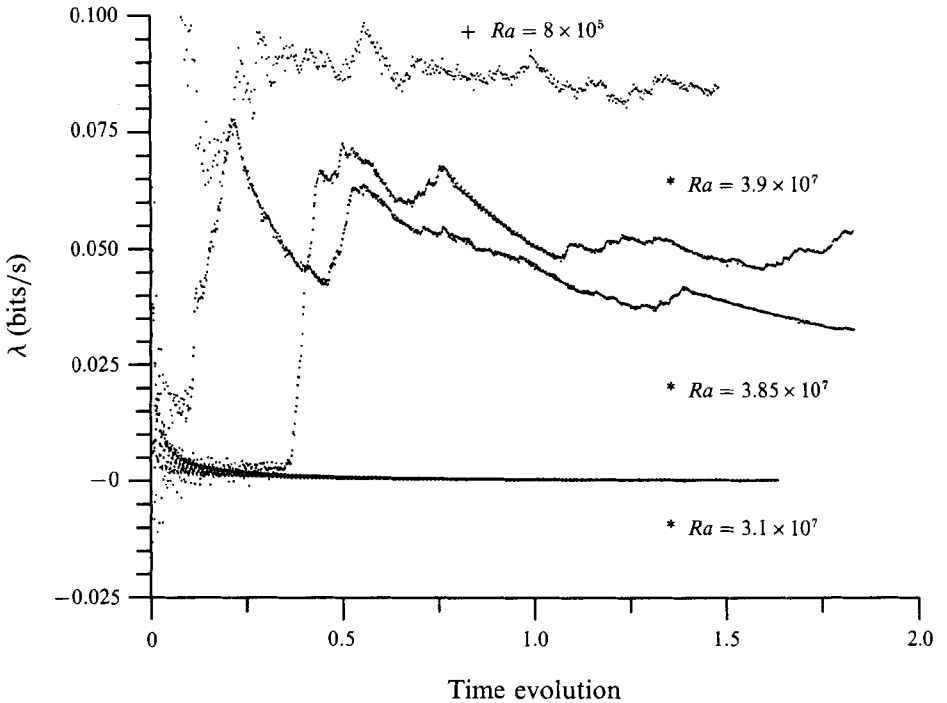

FIGURE 8. Temporal convergence of the leading Lyapounov exponent for various Rayleigh numbers: *, $A = 1$, $H_s = 0.75$; +, $A = 2$, $H_s = 1.75$.

during the laminar period and show excursions to other regions during the chaotic period. Figure 7(*b*) for the time point interval [197000–225000] exhibits anew the trajectories of the first burst period together with the next laminar period, the trajectories of which are moving back into the previous laminar region associated with the $\frac{4}{13}$ orbit, and then no differences are seen between figures 7(*a*) and 7(*b*). Similar behaviour has been found for $Ra = 3.9 \times 10^7$ and 4×10^7 but with an increase in broadband noise.

From their experiments, Forstrom & Sparrow (1967) reported turbulent bursts at the beginning of the transition between the laminar and turbulent states (note that Yosinobu *et al.* 1979 did not observe such phenomena). Always in the transition regime, Bill & Gebhart (1974) and Noto *et al.* (1982) recorded transits from a turbulent state back to a laminar one, which seems like an intermittency phenomenon.

From the above numerical results, it could be concluded that chaotic motion arises through a type-I intermittent transition. This type of intermittency is characterized by bursts of equal-magnitude periodic windows of identical frequencies, and near the transition the lengths of these windows vary in proportion to $(Ra - Ra_c)^{-\frac{1}{2}}$. The sequence of instabilities leading to non-periodic flows is also shown on table 4. The periodic two-frequency locked state has been abbreviated as P2T (Periodic motion on a 2-Torus) following Leibovich, Lele & Moroz (1989) who found a similar but more complex route to non-periodicity in Langmuir circulation with constrained motion.

4.4. *Lyapounov exponents*

One of the most useful diagnostic for chaotic systems is the study of the Lyapounov exponents which are related to the expanding and contracting nature of different directions in phase space. Indeed, one of the main characteristics of chaotic motion is

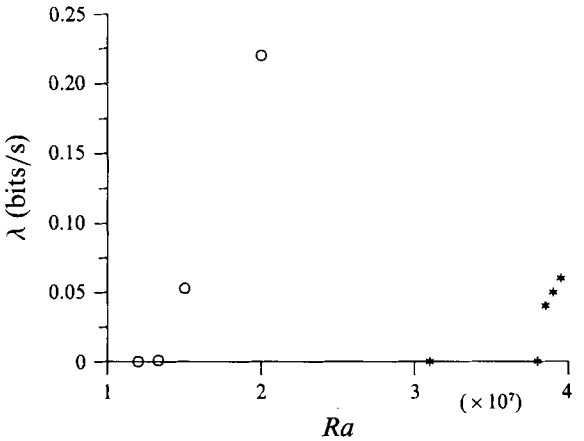

FIGURE 9. Leading Lyapounov exponents as a function of Rayleigh number for various configurations: *, $A = 1$, $H_s = 0.75$; ○, $A = 1$, $H_s = 0.50$.

the strong dependence of the solution on initial conditions. Thus, the largest Lyapounov exponent measures how unstable a given flow history is, and furthermore gives the timescale in which the system becomes unpredictable; in other words, the rate at which the system creates or destroys information (the exponents are expressed in bits of information per iteration). The sign of the Lyapounov exponents also provides a qualitative picture of a system's dynamics. An algorithm including a FORTRAN code for computing the leading Lyapounov exponent (LLE) from a discrete time series is given in Wolf *et al.* (1985) and has been improved by Wolf (1991, personal communication).

Figure 8 shows the temporal convergence of some LLE estimates for two geometrical configurations and various Ra values which carry the most important information about the dynamical behaviour of the system. Checks of the stationarity and exponent estimates with embedding dimension, delay time and evolution time between replacements have been performed to give confidence in our results. Some of the asymptotic values of the LLE are reported on figure 9 for various Rayleigh numbers and two different configurations. The periodicity of the flow found at $Ra = 3.1 \times 10^7$ is confirmed by the zero value of the LLE. For Rayleigh numbers greater than 3.8×10^7, the existence of one positive LLE implies the existence of chaotic behaviour and the larger the leading exponent is, the more the nearby trajectories diverge. This trend is well depicted on figures 8 and 9.

5. Penetrative convection

As can be seen on figure 1 (*b*), there is a stable layer of fluid at rest at the bottom of the vessel for small depths of immersion although the convective motion extends slightly below the line source. Computations have been carried out in square and in rectangular vessels. For a square vessel, penetrative convection occurs if the depth of immersion is such that $H_s \leqslant 0.5$ while for rectangular vessels it happens when the depth of immersion is smaller than the width of the cavity (i.e. $H_s \leqslant 1$). A map showing all the simulations carried out for $A = 2$ is given in figure 10 in which the symbols are for the different types of flows obtained.

The bifurcation points are supercritical Hopf points with low frequency. The dependence of the fluctuation amplitudes of the periodic motions on the Rayleigh number is given in figure 11 together with the evolution of the modified period ($Ra^{\frac{1}{2}}/f$),

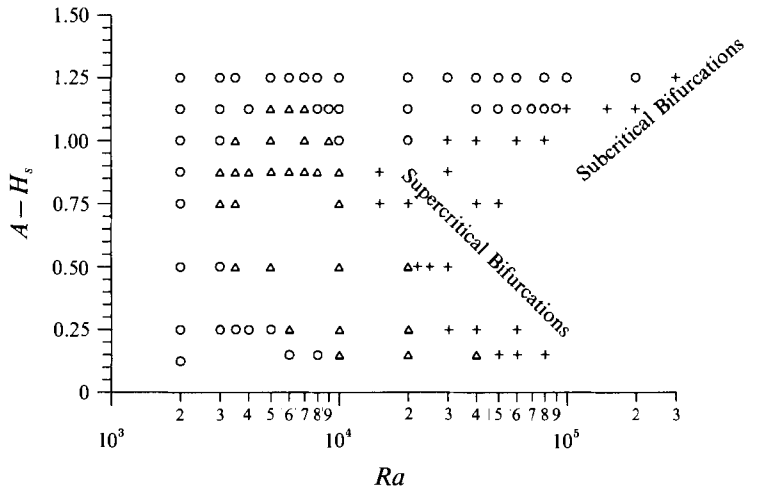

FIGURE 10. Summary of numerical simulations and flow regimes for vessels of aspect ratio 2: ○, symmetrical stationary motion; △, asymmetrical stationary motion; +, periodic motion.

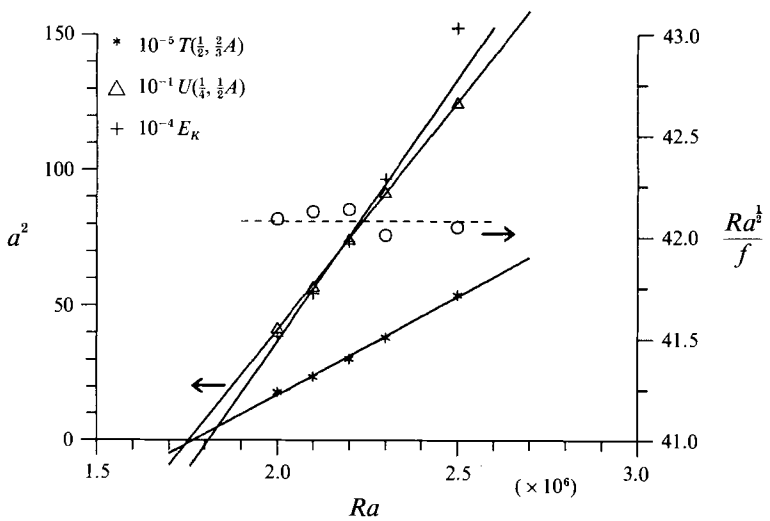

FIGURE 11. Variations of the squared amplitudes of fluctuations for horizontal components of the velocity U_2, temperature and mean kinetic energy.

while figure 12 contains information on the evolution of the critical frequency. It is clear from figure 11 that the limit-cycle bifurcation is supercritical in Rayleigh number. The amplitude increases roughly as the square root of the distance to the bifurcation point ($Ra \approx 1.75 \times 10^6$) and the modified period is almost constant. The low values of the frequencies found can be explained by the fact that the plume has to set in motion the fluid below the source. This is illustrated on figure 12(*a*) which shows a linear variation of the frequency of the critical points (given in table 3*c*) with the height of the layer below the source ($A - H_s$) for a constant depth of immersion, $H_s = 0.75$. Such a result clearly demonstrates that penetrative convection is the main phenomenon driving these instabilities. Furthermore, a $\frac{1}{2}$-power dependence of the frequency versus the critical Rayleigh numbers has also been found (figure 12*b*), indicating that near the threshold values internal gravity waves are present. Figure 13(*a*, *b*) shows the sustained

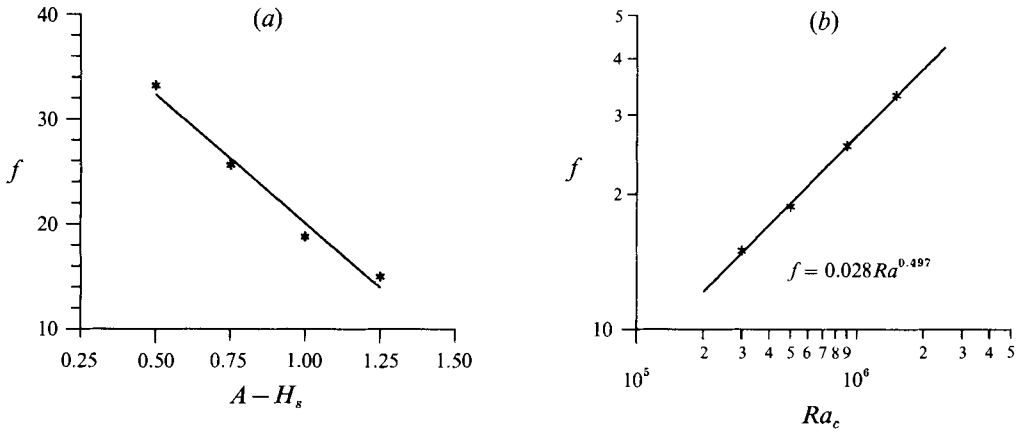

FIGURE 12. Variation of the frequency at critical points versus (*a*) height of layer below the source and (*b*) Rayleigh number for various aspect ratios and fixed depth of immersion $H_s = 0.75$.

oscillatory motion for $H_s = 0.5$ in a square cavity. The base-state streamlines (*a*) and isotherms (*b*) are plotted at the centre of figure 13(*a*, *b*). Snapshots of streamlines (*a*) and isotherms (*b*) are shown in counterclockwise progression around the figure at intervals of $\frac{1}{8}$ of one oscillation period. The two main vortices alternately penetrate below the line source at bottom. The twisting of the isotherms below the line source clearly depicts this motion. As mentioned earlier, some other cases in rectangular vessels and for depths of immersion $H_s \leqslant 1$ were investigated in a similar fashion. The same trends as for a square vessel were found and are not discussed here.

The periodic motion is characterized by a large contribution from the first two harmonics in the power spectra of the upper heat flux ϕ_1, as presented on figure 14(*a*). The flow then undergoes a second bifurcation into a limit cycle on a 2-torus. A weak frequency f_2, ten times smaller than the fundamental one f_1, appears at $Ra = 1.31 \times 10^7$ and a two-frequency locked state motion with a rotation number $r = f_2/f_1 = \frac{1}{10}$ is obtained. The phase portraits of the upper heat flux ϕ_1 with a 50 time-step lag displayed in figure 15 confirm this behaviour. Data are for the non-dimensional time interval [0.4, 1.64] which contains 7200 time points, and it should be noted that each limit cycle is made up of 67^+ time points. It can be seen that the trajectories are confined to a single curve with a cross-over for $Ra = 1.3 \times 10^7$ (figure 15*a*) while they are confined to what appears to be a 'ribbon' of roughly the same shape as before for $Ra = 1.33 \times 10^7$ (figure 15*b*). The spectra of the trajectories exhibit a large number of sidebands around the fundamental peak and its harmonics (figure 14*b*) resulting from a strong nonlinear interaction between the two locked frequencies, f_1 and f_2. As the Rayleigh number is increased, these sidebands develop further, both in number and amplitude and compete with one another (figure 14*c*). The phase portrait of figure 15(*c*) shows the thickening of the torus. The phase-space trajectories of the system remain confined to a two-torus over a narrow range of Rayleigh numbers, during which sidebands develop strongly in the spectrum. Figures 14(*d*) and 15(*d*) depict the system just after the onset of chaotic behaviour and show that the sidebands have grown throughout the spectrum, the underlying envelope being broadband, despite the sharpness of the fundamental frequency f_1 and its two first harmonics. This is exemplified by the phase space, which clearly shows that some periodic orbits are visited often (we can recognize roughly the same shape as the one shown in figure 15*a*), while the others appear aperiodic. Thus, this results in a fast transition to a fully chaotic spectrum.

(a)

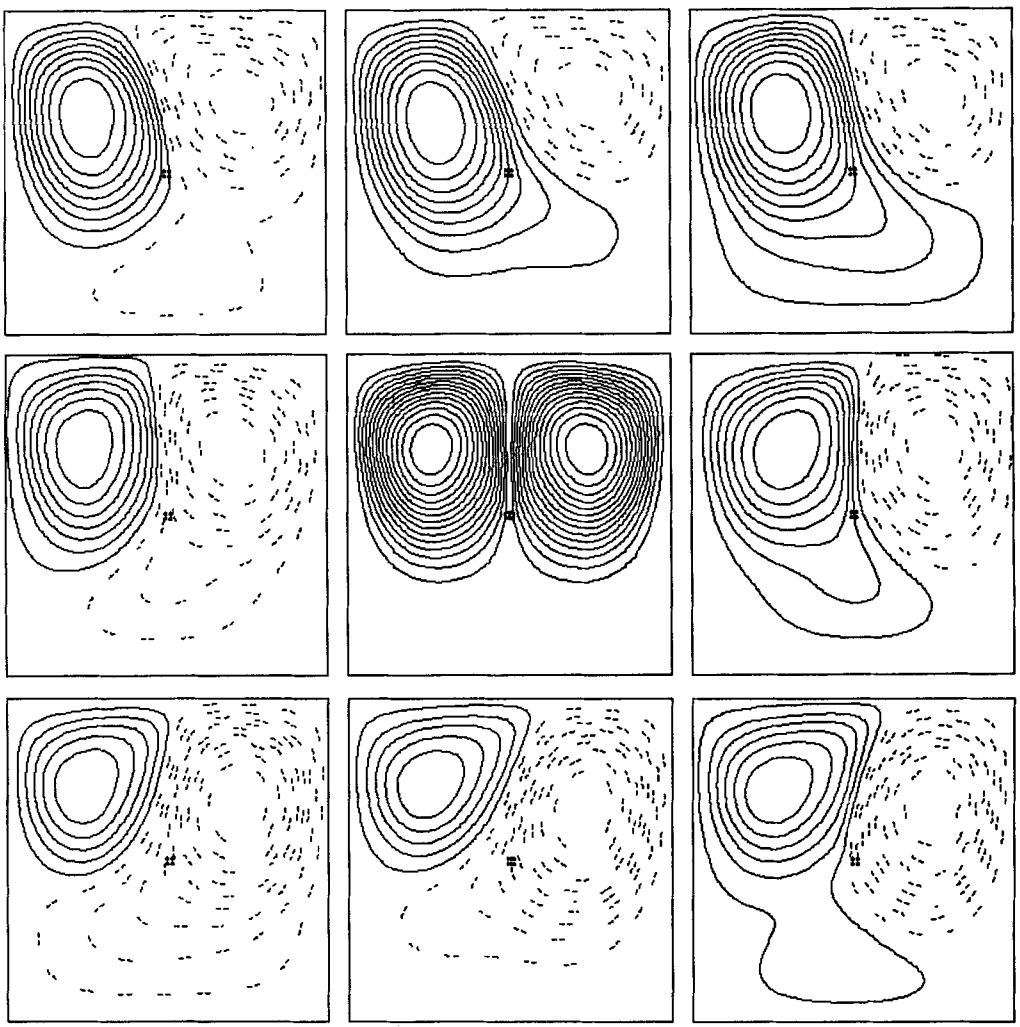

FIGURE 13(a). For caption see facing page.

As explained before, an objective measure of the degree of chaotic behaviour can be obtained by computing the LLE. Figure 9 confirms the previous results and depicts well the increasingly chaotic nature of the flow from $Ra = 1.35 \times 10^7$. But at $Ra = 1.3 \times 10^7$ the motion is always perfectly periodic, its LLE being zero.

Recently, Noto (1989) experimentally found that the swaying frequency is proportional to the 0.4 power of Rayleigh number for thermal plumes reaching the ceiling of the vessel in a laminar state. The aspect ratio of his experimental set-up was $A = 1.25$ with a dimensionless depth of immersion $H_s = 0.75$. For the same geometrical parameters, figure 16 depicts the evolution of the frequency versus the Rayleigh numbers and a power very close to Noto's has been found numerically, namely, 0.407. This gives us a high degree of confidence in our results. It must be noticed that the thermal boundary conditions play a minor role only. Indeed, in the experimental apparatus of Noto, the temperatures of the ceiling, the bottom and the four sidewalls were isothermally controlled while our numerical boundary conditions are imposed

(*b*)

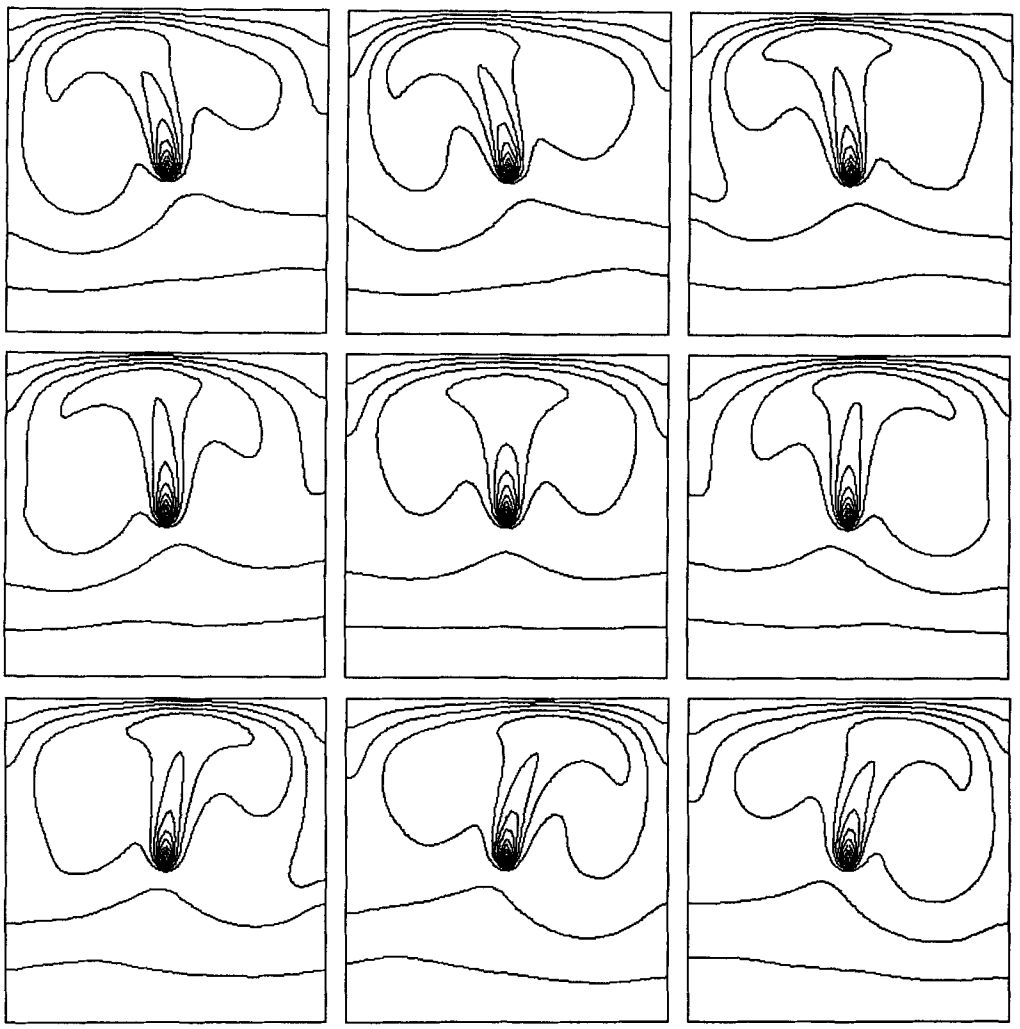

FIGURE 13. (*a*) Streamlines and (*b*) isotherms plotted over one oscillation period for $Ra = 2 \times 10^6$, $A = 1$, $H_s = 0.50$.

top and bottom temperatures and vertical adiabatic walls. We have also reported on figure 16 the frequencies found for vessels of different aspect ratios but with the same depth of immersion. As can be seen, the power is only slightly modified (0.433).

6. Rayleigh–Bénard-like convection

For rectangular vessels and depths of immersion greater than the width of the vessel ($H_s > 1$), very different bifurcations occur.

6.1. *Pitchfork bifurcation*

On increasing the Rayleigh number up to $Ra = 6000$, the symmetric two-cell pattern shown in figure 1(*c*) evolves towards an asymmetric one-cell pattern as displayed in figure 17. The plume is deflected towards one vertical adiabatic wall, either left or right

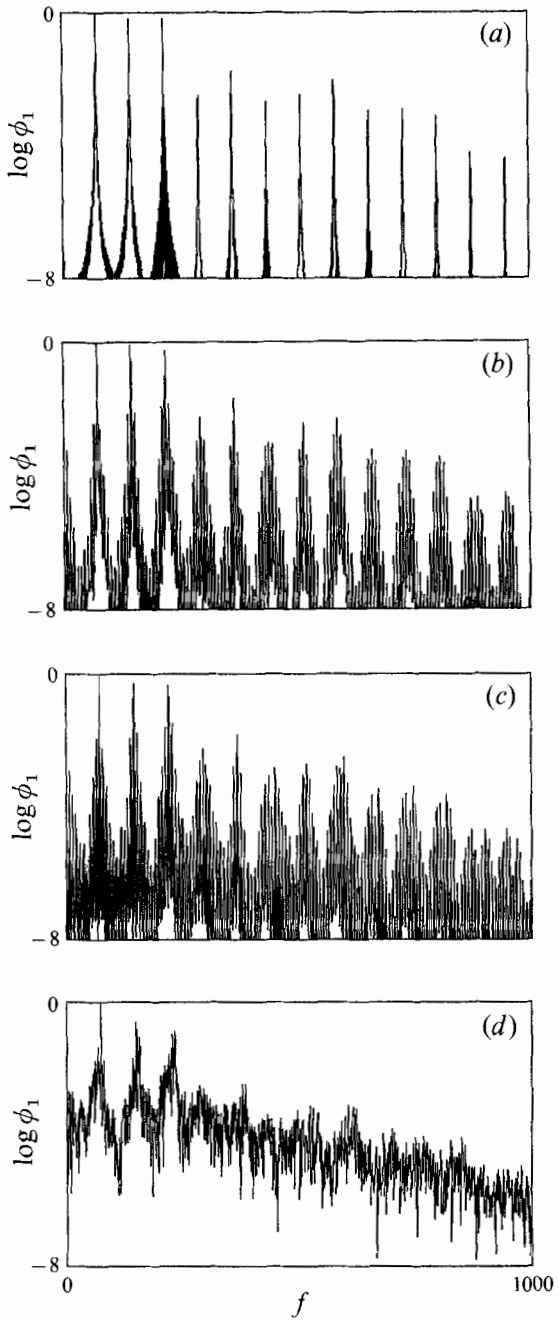

FIGURE 14. Power spectra for upper heat flux ϕ_1 in the left-half of a square vessel, $A = 1$, $H_s = 0.50$. (*a*) $Ra = 1.30 \times 10^7$, (*b*) $Ra = 1.33 \times 10^7$, (*c*) $Ra = 1.35 \times 10^7$, (*d*) $Ra = 1.50 \times 10^7$.

depending on the round-off errors generated during the computations. These two steady-state mirror-image solutions characterize a pitchfork bifurcation. It should be noticed that the symmetry breaking is not easy to observe because it arises after a long integration time. Indeed, all the criteria first satisfy machine convergence precision for a symmetric solution, then show substantial deviation and reach asymptotic values for asymmetric stationary flow.

Fujii *et al.* (1973) were the first to observe a deflection of the plume towards one of

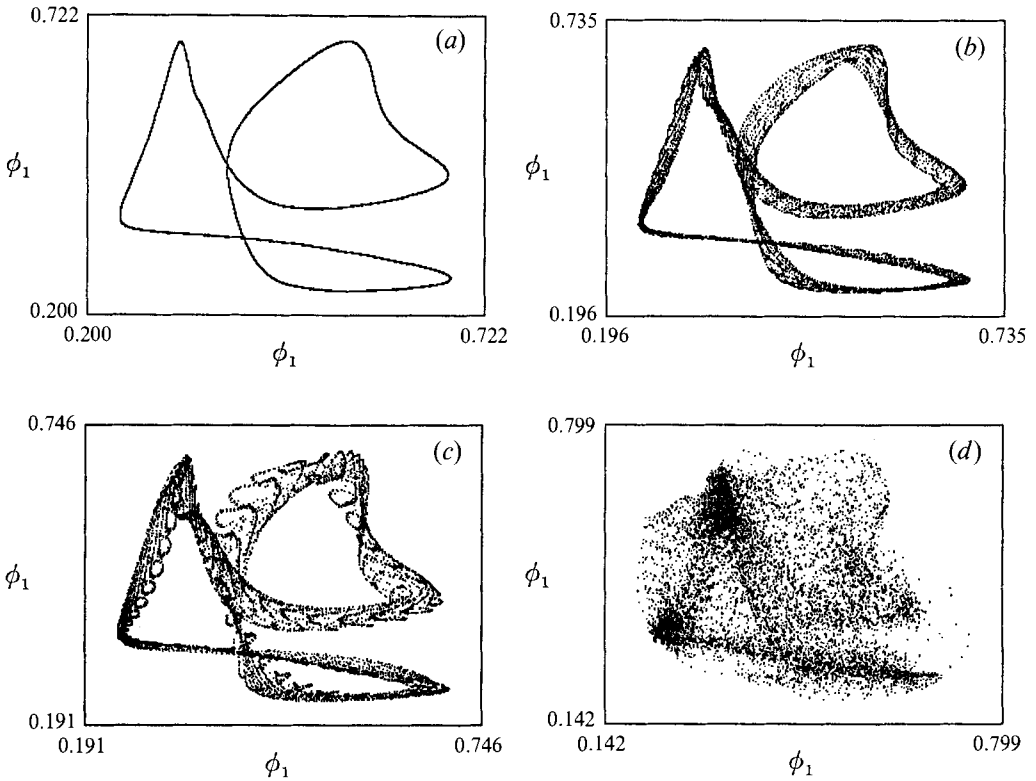

FIGURE 15. Phase portraits of upper heat flux ϕ_1 in the left-half of the vessel with a 50 time-step lag. (*a*) $Ra = 1.30 \times 10^7$, (*b*) $Ra = 1.33 \times 10^7$, (*c*) $Ra = 1.35 \times 10^7$, (*d*) $Ra = 1.50 \times 10^7$.

the walls when the temperatures of the vertical walls were slightly different. This deflection inhibits the swaying motion. Recently, some experimental studies devoted to plume interactions (Pera & Gebhart 1975; Incropera & Yaghoubi 1980), especially those on the interaction between a plume and a vertical unheated surface (Jaluria 1982), have shown that the basic mechanism of the deflection process is the limitation of the flow which supplies the fluid entrained downstream by the plume.

Contrary to what has been found for free laminar plumes, the destabilization of the two-cell flow comes from the unstably stratified layer of fluid at rest above the plume which appears when the plume does not reach the top of the vessel. Thus, Rayleigh–Bénard-like convection can arise in this upper layer when the Rayleigh number is high enough, giving way to one-cell flow which spreads out in the vessel. The potential for multiplicities of steady-state mirror solutions is the result of nonlinearities of the governing equations. A similar behaviour has been found by Hasnaoui, Bilgen & Vasseur (1990) for natural convection above an array of open cavities heated from below when the height of the vertical adiabatic confining walls is high enough.

6.2. *Subcritical Hopf bifurcation*

As the Rayleigh number is increased further, sustained oscillatory convection is obtained through a subcritical Hopf bifurcation. Convenient variables to describe the temporal evolution of the flow are local variables on the centreplane of the vessel. Figure 18(*a*) presents the evolution the horizontal velocity component U_1 at point $M_1(\frac{1}{2}, \frac{2}{3}A)$ for various Rayleigh numbers and for a depth of immersion $H_s = 1.75$. Below the pitchfork bifurcation point, which occurs at $Ra = 6 \times 10^3$, its value is zero due to

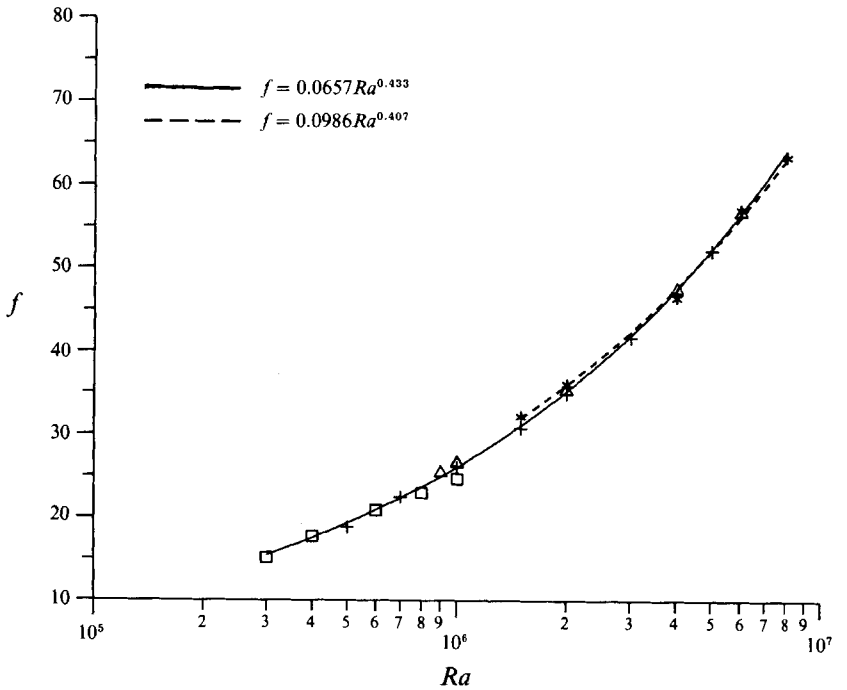

FIGURE 16. Evolution of the frequency for various aspect ratios (*, $A = 1.25$; △, $A = 1.50$; +, $A = 1.75$; □, $A = 2.00$) and depths of immersion: – – – –, best fit for $A = 1.25$, $H_s = 0.75$; ——, best fit for $H_s = 0.75$.

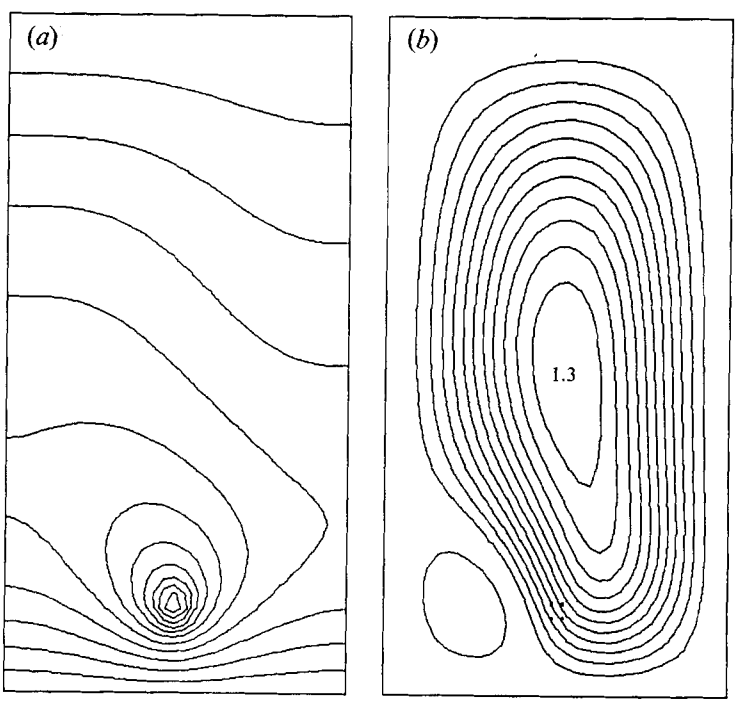

FIGURE 17. (*a*) Isotherms and (*b*) streamlines for stationary asymmetric flow, $A = 2$, $H_s = 1.75$, $Ra = 6 \times 10^3$.

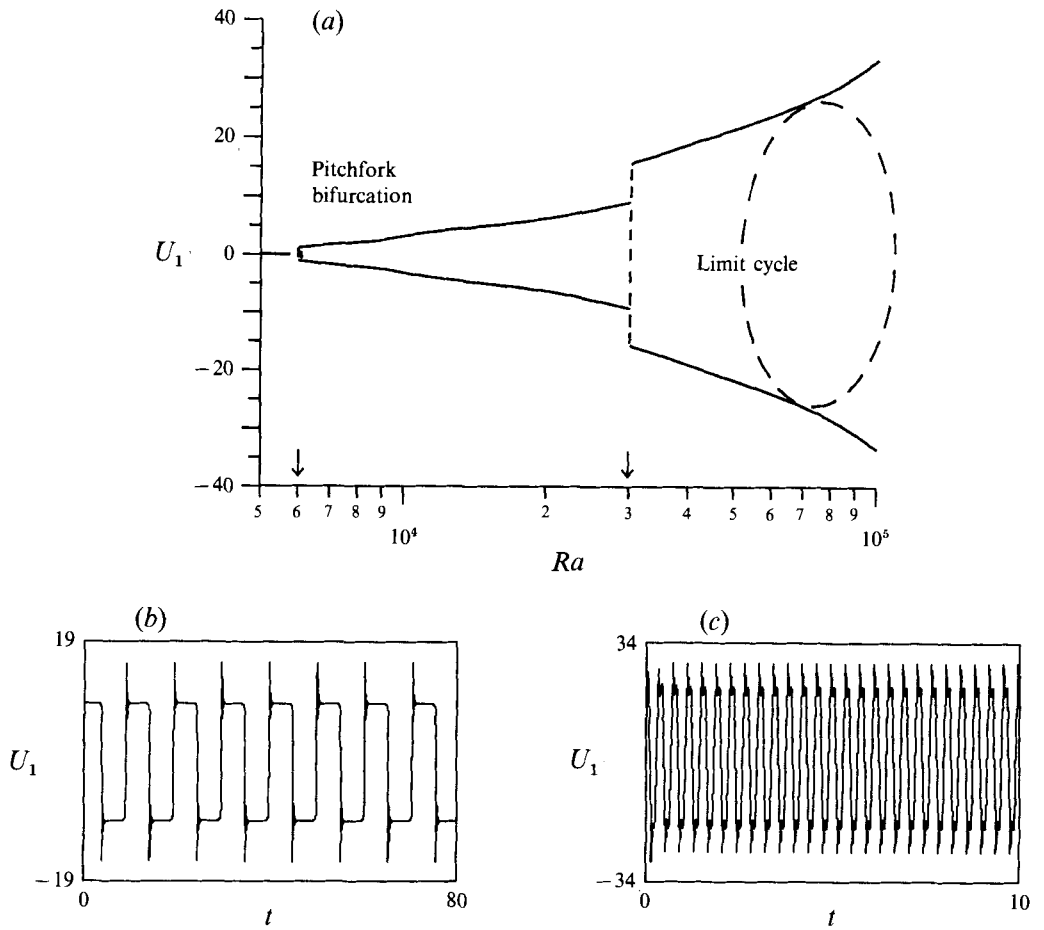

FIGURE 18. Evolution of the amplitude of the horizontal component of the velocity U_1: (*a*) for various Rayleigh numbers, (*b*) at $Ra = 3.02 \times 10^4$, (*c*) at $Ra = 8 \times 10^4$, $A = 2$, $H_s = 1.75$.

the flow symmetry. Above it the velocity component can take two opposite values. For higher Rayleigh numbers, the motion undergoes a second bifurcation at $Ra \approx 3.02 \times 10^4$ into a limit cycle and the value oscillates periodically between the two mirror values of the pitchfork bifurcation. Thus, oscillations onset with finite amplitude which defines a subcritical Hopf bifurcation. On decreasing the Rayleigh number from $Ra = 3.02 \times 10^4$ to 3.01×10^4 the flow became steady again. Consequently, no hysteresis effect was found. As can be seen in figure 18(*a*), the value of the horizontal component of the velocity jumps at the Hopf bifurcation point. The underlying phenomenon is clearly depicted on figure 18(*b*) which presents the time history of this variable for a Rayleigh number just above the onset of oscillations. Plateaux of opposite values, which are those of the pitchfork bifurcation, are periodically reached. The plume sways abruptly, overshoots briefly the other mirror flow solution due to its own inertia and becomes stable over a long period of time. At $Ra = 3.02 \times 10^4$ the period is equal to about 5 ($f \approx 0.2$). This is why the frequencies are so small for $H_s > 1$ (table 3*b*). On increasing the Rayleigh number, the solution continues to oscillate between two mirror solutions and the frequency is increased, the plateaux being shorter (figure 18*c*).

Figure 19 shows the streamlines (*a*) and isotherms (*b*) for $Ra = 4 \times 10^4$ in counterclockwise progression at an interval of $\frac{1}{8}$ of one oscillation period. Again, the base-state streamlines (*a*) and isotherms (*b*) are plotted at the centre of figure 19. The

(*a*)

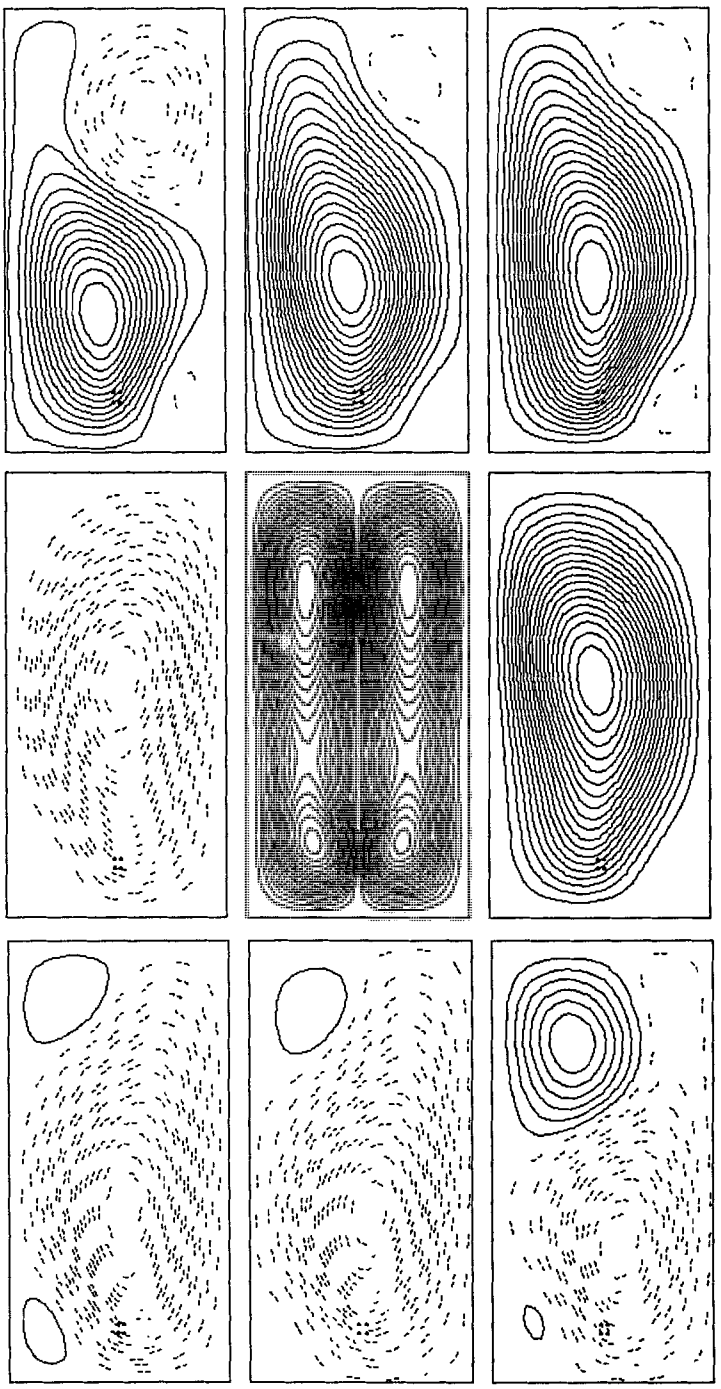

FIGURE 19(*a*). For caption see facing page.

periodic flow is characterized by three eddies: one primary vortex which rotates alternately clockwise and counterclockwise and occupies the central core, and two secondary eddies located near one of the vertical walls at the top and bottom corners. The top secondary eddy grows and finally occupies most of the vessel. Indeed, the fluid carried by this eddy becomes more and more cold on contact with the upper boundary,

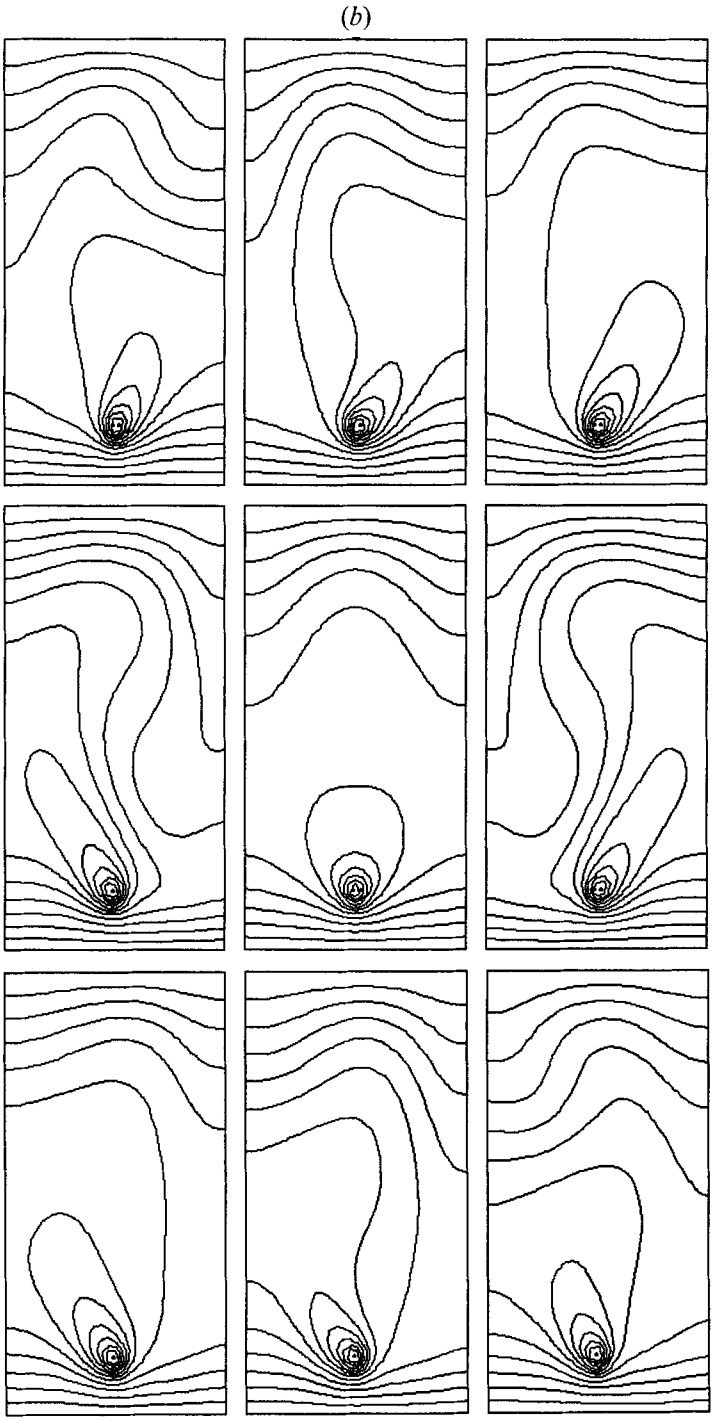

FIGURE 19. (*a*) Streamlines and (*b*) isotherms plotted over one oscillation period for $Ra = 4 \times 10^4$, $A = 2$, $H_s = 1.75$.

increasing its intensity, then collapses when the strength of the primary vortex is too weak to sustain it. Thus the plume is deflected towards the opposite vertical wall. Two secondary eddies then appear on the opposite vertical wall and a symmetrical evolution is observed. Figure 19 clearly depicts the oscillations of the periodic motion between

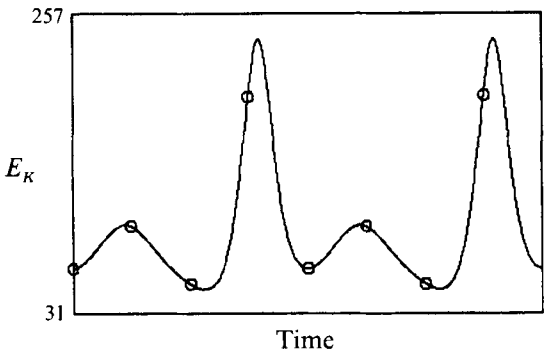

FIGURE 20. Time evolution of the mean kinetic energy during one oscillation period, $Ra = 4 \times 10^4$, $A = 2$, $H_s = 1.75$. Open circles correspond to the frames of figure 19.

the two asymmetric stationary solutions of the pitchfork branches. The physical mechanism behind the growth of the secondary upper eddy seems to be a separate flow-like process. Along one of the vertical boundary, the fluid first accelerates, then it slows down when encountering the upper boundary. This obstruction results in an increase in pressure. If the kinetic energy of the flow is too weak to negotiate this pressure hill, the flow separates and an eddy appears at the top corner, left or right, according to the direction of the circulation of the main stream. Indeed, as can be seen on figure 20, the kinetic energy dramatically increases twice in each period and the sharp peaks coincide with the absence of secondary eddies.

At higher Ra, it seems that the temporal behaviour of the oscillations becomes chaotic. The LLE estimate given in figure 8 shows that the motion is chaotic, at least for $Ra = 8 \times 10^5$. However, the regime is difficult to map accurately owing to limitations in the numerical resolution. Indeed, due to the very low value of the frequency, long time integrations are needed to correctly observe transitions and to obtain accurate power spectra. Nevertheless, it does not seem that any period-doubling scenario exists after the pitchfork bifurcation as for the classical Feigenbaum scenario.

7. Conclusions

Swaying motions of confined thermal plumes above a horizontal line heat source inside a vessel with adiabatic sidewalls, and cold top and bottom walls were numerically investigated and a variety of dynamic behaviour was shown according to the depth of immersion, aspect ratio and Rayleigh number.

For rectangular vessels with $A > 1$, two destabilizing mechanisms characterized by low-frequency motions were found:

(i) For depths of immersion greater than the width of the vessel and small enough Rayleigh numbers, Rayleigh–Bénard-like instability may appear within the layer of fluid above the thermal plume. The results obtained show asymmetric steady motions occurring through a pitchfork bifurcation, followed by a subcritical Hopf bifurcation. Twice over the period, one of the rolls is damped while the other occupies the whole vessel.

(ii) For depths of immersion smaller than the width, the mechanism driving the periodic motion is the penetrative convection which occurs within the layer of fluid at rest below the line heat source. The symmetric plume rolls may destabilize this layer and then penetrate alternately to the bottom through a soft bifurcation (Hopf point).

In these cases, two convection rolls of almost same strength always exist over all the period.

For square vessels ($A = 1$), penetrative convection could be seen for quite small depths of immersion. On the other hand, an upper unstable layer at rest was found even for a line source located close to the bottom of the vessel. In these cases, steady symmetric flows exist at high Rayleigh numbers. For Ra greater than a critical value, which depends on the depth of immersion, a swaying motion with high frequency starts. This motion is followed by a two-frequency locked regime, then a weakly turbulent regime arises via an intermittent route to chaos.

In the past, a number of experiments have been conducted for freely rising plumes in air at atmospheric pressure with the aim of clarifying the transition between the laminar and turbulent regimes. Some experiments have been done using large enclosures, but the geometrical dimensions were not fully specified generally. Thus, comprehensive comparisons with the present results are difficult. A comparison with the experimental correlation given by Noto (1989) for the swaying frequency of laminar plumes is discussed in the present paper. It has been found that the numerical predictions are in very good agreement with the experimental frequency for an aspect ratio $A = 1.25$ and a depth of immersion $H_s = 0.75$.

The authors are grateful for the support provided by the Centre de Compétence en Calcul Numérique Intensif (C3NI), Ministère de l'Education Nationale-IBM agreement, through the use of the IBM 3090-600/VF at the Centre National Universitaire Sud de Calcul (CNUSC, Montpellier, France).

REFERENCES

BECK, J. V., MCLAIN, H. A., KARNITZ, M. A., SHONDER, J. A. & SEGAN, E. G. 1988 Heat losses from underground steam pipes. *Trans. ASME* C: *J. Heat Transfer* **110**, 814–820.

BÉRGE, P., POMEAU, Y. & VIDAL, CH. 1988 *L'Ordre Dans le Chaos*. Hermann.

BILL, R. G. & GEBHART, B. 1975 The transition of plane plumes. *Intl J. Heat Mass Transfer* **18**, 513–526.

BRODOWICZ, K. & KIERKUS, W. T. 1966 Experimental investigation of laminar free-convection flow in air above horizontal wire with constant heat flux. *Intl J. Heat Mass Transfer* **9**, 81–94.

DESRAYAUD, G., LEPEUTREC, Y. & LAURIAT, G. 1990 Numerical simulation of oscillatory convection in low-*Pr* fluids. In *Notes on Numerical Fluid Mechanics*, vol. 27, pp. 49–56. Vieweg.

EICHHORN, R., LIENHARD, J. H. & CHEN, C. C. 1974 Natural convection from isothermal spheres and cylinders immersed in a stratified fluid. In *Proc. 5th Intl Heat Transfer Conf., Tokyo*, JSME–SCEJ, vol. 3, pp. 10–14.

EICHHORN, R. & VEDHANAYAGAM, M. 1982 The swaying frequency of line source plumes. In *Proc. 7th Intl Heat Transfer Conf., Munich* (ed. U. Grigull, E. Hahne, K. Stephan & J. Straub), vol. 2, pp. 407–412. Hemisphere.

FORSTROM, R. J. & SPARROW, E. M. 1967 Experiments on the buoyant plumes above a heated horizontal wire. *Intl J. Heat Mass Transfer* **10**, 321–331.

FUJII, T. 1963 Theorey of the steady laminar natural convection above a horizontal line heat source and a point heat source. *Intl J. Heat Mass Transfer* **6**, 597–606.

FUJII, T., MORIOKA, I. & UEHARA, H. 1973 Buoyant plume above horizontal line heat source. *Intl J. Heat Mass Transfer* **16**, 755–768.

GEBHART, B., JALURIA, Y., MAHAJAN, R. L. & SAMMAKIA, B. 1988 *Buoyancy-Induced Flows and Transport*. Springer.

GEBHART, B., PERA, L. & SCHORR, A. W. 1970 Steady laminar natural convection plumes above a horizontal line heat source. *Intl J. Heat Mass Transfer* **13**, 161–171.

HAALAND, S. E. & SPARROW, E. M. 1973 Stability of buoyant boundary layers and plumes, taking into account of nonparallelism of the basic flows. *Trans. ASME* C: *J. Heat Transfer* **95**, 295–301.

HASNAOUI, M., BILGEN, E. & VASSEUR, P. 1990 Natural convection above an array of open cavities heated from below. *Numer. Heat Transfer* **18A**, 463–482.

HIEBER, C. A. & NASH, E. J. 1975 Natural convection above a line heat source: higher-order effects and stability. *Intl J. Heat Mass Transfer* **18**, 1473–1479.

INCROPERA, F. P. & YAGHOUBI, M. A. 1980 Buoyancy driven flows originating from heated cylinders submerged in a finite water layer. *Intl J. Heat Mass Transfer* **23**, 269–278.

JALURIA, Y. 1982 Thermal plume interaction with vertical surfaces. *Lett. Heat Mass Transfer* **9**, 107–117.

LAURIAT, G. & DESRAYAUD, G. 1990 Numerical study of oscillatory buoyant plumes above a horizontal line heat source. In *Proc. 9th Intl Heat Transfer Conf., Jerusalem* (ed. G. Hetsroni), vol. 4, pp. 171–176. Hemisphere.

LEIBOVICH, S., LELE, S. K. & MOROZ, I. M. 1989 Nonlinear dynamics in Langmuir circulations and thermosolutal convection. *J. Fluid Mech.* **198**, 471–511 (and Corrigendum **235** (1992), 690).

LYAKHOV, Y. N. 1970 Experimental investigation of free convection above a heated horizontal wire. *J. Appl. Mech. Tech. Phys.* **11**, 355–359.

MÖRWALD, K., MITSOTAKIS, K. & SCHNEIDER, W. 1986 Higher-order analysis of laminar plumes. In *Proc. 8th Intl Heat Transfer Conf., San Francisco* (ed. C. L. Tien, V. P. Carrey & J. K. Ferrell), vol. 3, pp. 1335–1340. Hemisphere.

NAWOJ, H. J. & HICKMAN, R. S. 1977 An experimental investigation of the plume velocity field above a horizontal line heat source. *Trans. ASME* C: *J. Heat Transfer* **99**, 609–613.

NOTO, K. 1989 Swaying motion in thermal plume above a horizontal line heat source. *J. Thermophys.* **3**, 428–434.

NOTO, K., MATSUI, S. & MATSUMOTO, R. 1982 Observation on vortex pair of plane plume in thermally stratified fluid. In *Flow Visualization*, vol. 4, pp. 697–702. Springer.

PERA, L. & GEBHART, B. 1971 On the stability of laminar plumes: some numerical solutions and experiments. *Intl J. Heat Mass Transfer* **14**, 975–984.

PERA, L. & GEBHART, B. 1975 Laminar plume interactions. *J. Fluid Mech.* **68**, 259–271.

PEYRET, R. 1990 The Chebyshev multidomain approach to stiff problems in fluid mechanics. *Comput. Methods Appl. Mech. Engng* **80**, 129–145.

SCHORR, A. W. & GEBHART, B. 1970 An experimental investigation of natural convection wakes above a line heat source. *Intl J. Heat Mass Transfer* **13**, 557–571.

URAKAWA, K., MORIOKA, I. & KIYOTA, M. 1983 Swaying motion of the buoyant plume above a horizontal line heat source. In *Proc. 1st ASME-JSME Thermal Engng Conf., Honolulu.* HI, vol. 3, pp. 215–220.

WAKITANI, S. 1985 Non-parallel-flow stability of a two-dimensional buoyant plume. *J. Fluid Mech.* **159**, 241–258.

WAKITANI, S. & YOSINOBU, H. 1984 Stability characteristics of a natural convection flow above a horizontal line heat source. *J. Phys. Soc. Japan* **53**, 1291–1300.

WOLF, A., SWIFT, J. B., SWINNEY, H. L. & VASTANO, J. A. 1985 Determining Lyapounov exponents from a time series. *Physica* **16D**, 285–317.

YAGHOUBI, M. A. & INCROPERA, F. P. 1978 Natural convection from a heated horizontal cylinder submerged in a shallow water layer. In *Proc. 6th Intl Heat Transfer Conf., Toronto*, vol. 2, pp. 269–274. Hemisphere.

YOSINOBU, H., ONISHI, Y., AMANO, S., ENYO, S. & WAKITANI, S. 1979 Experimental study on instability of a natural convection flow above a horizontal line heat source. *J. Phys. Soc. Japan* **47**, 312–319.

ZIA, J. L., XIN, M. D. & ZHANG, H. J. 1990 Natural convection in an externally heated enclosure containing a local heat source. *J. Thermophys.* **4**, 233–238.